



Viscoplastic sheets and threads

N.J. Balmforth^{a,b,*}, I.J. Hewitt^a

^a Department of Mathematics, University of British Columbia, Vancouver, BC, Canada V6T 1Z2

^b Department of Earth & Ocean Science, University of British Columbia, Vancouver, BC, Canada V6T 1Z2

ARTICLE INFO

Article history:

Available online 13 June 2012

Keywords:

Viscoplastic fluids
Bending and buckling theory
Mathematical modelling

ABSTRACT

A theory is presented for the dynamics of slender sheets of viscoplastic fluid. First a model suitable for relatively small curvature is presented and applied to the fall of a liquid bridge supported at its two ends. Second, order-one curvatures are considered, along with the sagging of a beam with a free end that is either emplaced or extruded horizontally. We then present a theory combining both limits of curvature, and consider the buckling of a nearly vertical column. Analogous models for a circular viscoplastic thread are also discussed.

© 2012 Elsevier B.V. All rights reserved.

1. Introduction

An everyday vision of viscoplastic fluid dynamics is afforded whenever one squeezes toothpaste out of a tube. The paste initially emerges from the tube as a solid cylinder, before yielding under gravity and fluidly bending downwards; eventually the paste forms a distinctively curved thread. Alternatively, squeezing the toothpaste vertically upwards creates an upright column that suffers a form of Euler buckling once its height exceeds some limit (Fig. 1). Similar viscoplastic extrusions feature in a number of other household and industrial fluid problems ranging from the caulking gun to manufacturing and food processing.

In solid mechanics, the problem of a sagging or dangling elastic thread has a rich history dating back to Galileo, and theory for bending of beams and rods is well developed [7]. The essential premise of the theory is that the slenderness of the geometry of the sheet or thread can be exploited to simplify the governing equations of linear (or even nonlinear) elasticity and furnish a reduced model determining the deflection as a function of time and arc length along the central axis. The extension of this theory to perfectly plastic sheets and rods was popular in the mid 1900s [10,8], although most attention seems to have been directed at the contained (i.e. spatially confined) plastic deformation of elastic–plastic beams and the determination of the limit for failure (the onset of unconfined plastic flow). A relevant exception is the body of work on the impact loading of plastic beams by a suddenly applied force, and the determination of the degree of permanent deformation thereby suffered (see [8], Section 7).

* Corresponding author at: Department of Mathematics, University of British Columbia, Vancouver, BC, Canada V6T 1Z2.

E-mail address: njb@math.ubc.ca (N.J. Balmforth).

The analogous theory for viscous sheets and threads was presented only much more recently, and catalyzed in part by the analogy between Stokes flow and elasticity (e.g. [14,4,11,15]). In this context, flow problems much like the bending of extruded toothpaste have been considered. Notable examples include the sagging and extrusion of viscous beams ([11]; the analogues of Galileo's cantilever and the “reverse spaghetti problem”), the falling viscous catenary [15,6], the folding of viscous sheets [9,12], and the coiling of syrup [13].

Our goal in the current work is to provide the equivalent of these solid and fluid mechanical theories for a slender viscoplastic sheet or thread. In Section 2, we begin the mathematical discussion by formulating a theory for a two-dimensional sheet of Herschel–Bulkley fluid with relatively small curvature. We then apply this theory to the problem of the viscoplastic catenary – our version of the solid mechanical problem posed by Bernoulli centuries ago. The viscous version of this problem was studied in [15], and a related study with a visco–elasto–plastic rheology was recently carried out in [5]. In Section 3, we continue on to explore larger deflections of the sheet, focussing on the Bingham fluid. The order-one curvature theory is then applied to study the sagging of a viscoplastic beam with a free end, with the beam either emplaced horizontally to begin with (i.e. the viscoplastic counterpart of Galileo's problem), or extruded horizontally (as in Ribe's model of subducting slabs [12]). Section 4 continues the discussion by outlining a higher-order formulation that combines the small and order-one curvature theories, in addition to capturing the dynamics of sheets undergoing pure extension and no bending. That theory is then applied to the analogue of the Euler buckling problem, the failure and collapse of a viscoplastic column extruded almost vertically. In the appendix we present a complementary discussion of axisymmetric viscoplastic threads, and recover an essentially equivalent theory. Thus, most of our results apply equally to threads as well as sheets.



Fig. 1. Top row: a horizontal extrusion of “Sensodyne Whitening” toothpaste. The photographs are four seconds apart. Lower left: an extrusion of “Neosporin” (images are 2, 2 and 3 seconds apart). Lower right: extruding the Sensodyne toothpaste vertically, with images 1 and 0.5 seconds apart.

2. Viscoplastic sheets and the drooping catenary

2.1. Dimensional formulation

Consider a thin sheet of a viscoplastic fluid described by the Herschel–Bulkley constitutive model, deforming due to surface tension and the body force of gravity. The geometry is sketched in Fig. 2. In this section, the sheet undergoes small deflections of order its thickness and, as in classical beam theory, it is convenient to use the Cartesian coordinate system (x, z) orientated with the horizontal. The velocity field in these coordinates is (u, w) , pressure is p , and the components of the total and deviatoric stress tensors are denoted $\sigma_{ij} \equiv \tau_{ij} - p\delta_{ij}$ and τ_{ij} , respectively.

The governing equations are conservation of mass and momentum,

$$\frac{\partial u}{\partial x} + \frac{\partial w}{\partial z} = 0, \quad (1)$$

$$\rho \left(\frac{\partial u}{\partial t} + u \frac{\partial u}{\partial x} + w \frac{\partial u}{\partial z} \right) = \frac{\partial \sigma_{xx}}{\partial x} + \frac{\partial \sigma_{xz}}{\partial z}, \quad (2)$$

$$\rho \left(\frac{\partial w}{\partial t} + u \frac{\partial w}{\partial x} + w \frac{\partial w}{\partial z} \right) = \frac{\partial \sigma_{xz}}{\partial x} + \frac{\partial \sigma_{zz}}{\partial z} - \rho g \quad (3)$$

where ρ is the fluid density, t is time, and g is gravity. The constitutive model may be written in the form

$$\tau_{ij} = \left(K \dot{\gamma}^{n-1} + \frac{\tau_Y}{\dot{\gamma}} \right) \dot{\gamma}_{ij} \quad \text{if } \tau > \tau_Y, \quad (4)$$

and $\dot{\gamma}_{ij} = 0$ otherwise, where

$$\dot{\gamma}_{xx} = -\dot{\gamma}_{zz} = 2 \frac{\partial u}{\partial x}, \quad \dot{\gamma}_{xz} = \frac{\partial u}{\partial z} + \frac{\partial w}{\partial x}, \quad (5)$$

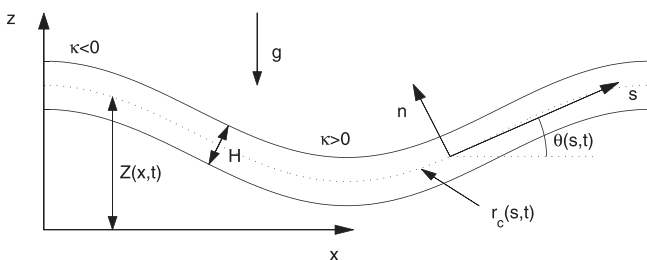


Fig. 2. A sketch of the geometry. The sheet is described by the Cartesian coordinates (x, z) in Section 2, and by the curvilinear coordinates (s, n) in Section 3.

and the second invariants are $\tau = \sqrt{\tau_{xx}^2 + \tau_{zz}^2}$ and $\dot{\gamma} = \sqrt{\dot{\gamma}_{xx}^2 + \dot{\gamma}_{zz}^2}$. Here K , n and τ_Y are rheological parameters, the latter being the yield stress.

The upper and lower surfaces of the fluid are located at $z = Z_{\pm}(x, t) = Z \pm \frac{1}{2}H \sec \theta$, where $z = Z(x, t)$ denotes the midline, $H(x, t)$ is the thickness, and $\theta(x, t)$ is the angle the midline makes with the horizontal (see Fig. 2). The kinematic conditions are

$$\frac{\partial Z_{\pm}}{\partial t} + u(x, Z_{\pm}, t) \frac{\partial Z_{\pm}}{\partial x} = w(x, Z_{\pm}, t). \quad (6)$$

The internal stresses generate forces on these surfaces,

$$\frac{1}{\sqrt{1 + (\partial Z_{\pm} / \partial x)^2}} \begin{pmatrix} \sigma_{xz} - \sigma_{xx} \partial Z_{\pm} / \partial x \\ \sigma_{zz} - \sigma_{zz} \partial Z_{\pm} / \partial x \end{pmatrix}, \quad (7)$$

which are countered by the interfacial forces,

$$\pm \frac{\gamma \partial^2 Z_{\pm} / \partial x^2}{[1 + (\partial Z_{\pm} / \partial x)^2]^{3/2}} \begin{pmatrix} -\partial Z_{\pm} / \partial x \\ 1 \end{pmatrix}, \quad (8)$$

where γ is the surface tension.

Depending upon the specific problem under consideration, the ends of the sheet may have prescribed stresses, displacement or velocity; we defer prescription of these end conditions, as well as the initial state of the sheet, until later when we consider explicit examples.

2.2. Scaling

The slenderness of the sheet implies that $\epsilon = \mathcal{H} / \mathcal{L} \ll 1$, where \mathcal{H} is a typical thickness of the undeformed sheet and \mathcal{L} is a characteristic horizontal scale. We use these two scales to non-dimensionalize lengths, and introduce a characteristic vertical speed scale, \mathcal{U} , and extensional stress, \mathcal{S} , to remove dimensions from the velocity field, time and stresses:

$$x = \mathcal{L} \hat{x}, \quad (z, Z, Z_{\pm}, H) = \mathcal{H}(\hat{z}, \hat{Z}, \hat{Z}_{\pm}, \hat{H}), \quad (9)$$

$$(u, w) = \mathcal{U}(\epsilon \hat{u}, \hat{w}), \quad t = \mathcal{U}^{-1} \mathcal{H} \hat{t}, \quad (10)$$

$$(p, \sigma_{xx}, \sigma_{xz}, \sigma_{zz}) = \mathcal{S}(\hat{p}, \hat{\sigma}_{xx}, \epsilon \hat{\sigma}_{xz}, \epsilon^2 \hat{\sigma}_{zz}), \quad (11)$$

$$(\tau_{xx}, \tau_{xz}, \tau_{zz}) = \mathcal{S}(\hat{\tau}_{xx}, \epsilon \hat{\tau}_{xz}, \hat{\tau}_{zz}), \quad (12)$$

so that the dimensionless variables are distinguished by their hats. The rate-dependent part of the constitutive law motivates choosing the stress scale to be

$$S = K \left(\frac{\epsilon \mathcal{U}}{\mathcal{L}} \right)^n. \quad (13)$$

The specific scaling of the various velocity and stress components is guided by the analogous theory for a Newtonian sheet [3,4,11].

With these choices, the continuity Eq. (1) becomes

$$\frac{\partial \hat{u}}{\partial \hat{x}} + \frac{1}{\epsilon^2} \frac{\partial \hat{w}}{\partial \hat{z}} = 0, \quad (14)$$

in view of which we set

$$\hat{w} = \widehat{W}(x, t) + O(\epsilon^2). \quad (15)$$

On discarding the hat decoration and retaining only the leading order terms, the momentum equations take the dimensionless form,

$$0 = \frac{\partial \sigma_{xx}}{\partial x} + \frac{\partial \sigma_{xz}}{\partial z}, \quad (16)$$

$$\text{Re} \frac{\partial W}{\partial t} = \frac{\partial \sigma_{xz}}{\partial x} + \frac{\partial \sigma_{zz}}{\partial z} - G, \quad (17)$$

and the constitutive law reduces to

$$\tau_{xx} = 2\dot{\gamma}^{n-1} \frac{\partial u}{\partial x} + B \text{sgn} \left(\frac{\partial u}{\partial x} \right), \quad \dot{\gamma} = 2 \left| \frac{\partial u}{\partial x} \right|, \quad (18)$$

for $|\tau_{xx}| > B$, and $|\partial u / \partial x| = 0$ otherwise. The dimensionless parameters are

$$\text{Re} = \frac{\rho \mathcal{L}^2 \mathcal{U}^2}{\mathcal{H}^2 S}, \quad G = \frac{\rho g \mathcal{H}}{\epsilon^2 S} \quad \text{and} \quad B = \frac{\tau_Y}{K} \left(\frac{\mathcal{L}}{\epsilon \mathcal{U}} \right)^n, \quad (19)$$

representing measures of inertia, gravity and yield stress. Below, we will be primarily interested in situations in which the Reynolds number, Re, is not important, and focus chiefly on studying the effect of varying the gravity parameter, G, and Bingham number, B.

The smaller scaling of $\sigma_{xz} = \tau_{xz}$ in (4) and (5) implies that

$$\frac{\partial u}{\partial z} + \frac{\partial W}{\partial x} = 0. \quad (20)$$

Moreover, because σ_{zz} is also scaled to be small, $\tau_{zz} - p = O(\epsilon^2)$, indicating

$$p = \tau_{zz} = -\tau_{xx} \quad \text{and} \quad \sigma_{xx} = 2\tau_{xx}. \quad (21)$$

Finally, the boundary conditions become

$$\frac{\partial Z_+}{\partial t} = \frac{\partial Z_-}{\partial t} = W, \quad (22)$$

$$\sigma_{xz} - \sigma_{xx} \frac{\partial Z_{\pm}}{\partial x} = 0, \quad (23)$$

$$\sigma_{zz} - \sigma_{xz} \frac{\partial Z_{\pm}}{\partial x} = \pm \Gamma \frac{\partial^2 Z_{\pm}}{\partial x^2}, \quad (24)$$

where

$$\Gamma = \frac{\gamma}{\epsilon \mathcal{L} S}. \quad (25)$$

Thus, in view of our scalings,

$$Z_{\pm} = Z \pm \frac{1}{2} H, \quad (26)$$

and H is fixed in time (and given by the initial state).

2.3. Reduction

We now integrate (16) and (17) in z and use (23) and (24):

$$\frac{\partial \Sigma}{\partial x} = 0, \quad (27)$$

and

$$\text{Re} H \frac{\partial W}{\partial t} = \frac{\partial Q}{\partial x} + 2\Gamma \frac{\partial^2 Z}{\partial x^2} - GH, \quad (28)$$

where Σ and Q are the stress resultants,

$$\Sigma = \int_{Z-\frac{1}{2}H}^{Z+\frac{1}{2}H} \sigma_{xx} dz \quad \text{and} \quad Q = \int_{Z-\frac{1}{2}H}^{Z+\frac{1}{2}H} \sigma_{xz} dz. \quad (29)$$

After multiplying (16) by $(z - Z)$, a similar integral furnishes

$$\frac{\partial M}{\partial x} + \Sigma \frac{\partial Z}{\partial x} = Q, \quad (30)$$

where the effective moment is

$$M = \int_{Z-\frac{1}{2}H}^{Z+\frac{1}{2}H} (z - Z) \sigma_{xx} dz. \quad (31)$$

Consequently, eliminating Q,

$$\text{Re} H \frac{\partial W}{\partial t} = \frac{\partial^2 M}{\partial x^2} + (\Sigma + 2\Gamma) \frac{\partial^2 Z}{\partial x^2} - GH. \quad (32)$$

Aside from some guidance in the choice of asymptotic scalings, the constitutive law has not yet played any role. However, σ_{xx} must still be connected to the leading-order vertical velocity W. Condition (20) assists in part:

$$u \approx U(x, t) - (z - Z) \frac{\partial W}{\partial x}, \quad (33)$$

where $U(x, t)$ is the horizontal midline velocity. That is,

$$\frac{\partial u}{\partial x} = \Delta - (z - Z) W_{xx}, \quad (34)$$

where

$$\Delta = U_x + Z_x W_x \quad (35)$$

and subscripts on U , W and Z denote partial derivatives. To proceed further, we must first decide where the fluid is yielded and where it is rigid. The fluid is locally unyielded if there is a range of z with $\partial u / \partial x = 0$. From (34), we observe that this demands both $\Delta = 0$ and $W_{xx} = 0$. But then $\partial u / \partial x = 0$ across the entire sheet in this particular cross-section, so for a given horizontal position, the sheet must be either fully yielded or rigid across its thickness. For the yielded sections, (18), (21) and (34) give

$$\sigma_{xx} = 2(|\dot{\gamma}_{xx}|^n + B) \text{sgn}(\dot{\gamma}_{xx}), \quad (36)$$

with

$$\dot{\gamma}_{xx} = 2\Delta - 2(z - Z)W_{xx}, \quad (37)$$

We may now construct the resultant stress and moment: if the sheet is yielded,

$$\Sigma = \frac{H^n |W_{xx}|^{n-1} W_{xx}}{n+1} (|1 + \check{\Xi}|^{n+1} - |1 - \check{\Xi}|^{n+1}) + 2BH\Xi \text{sgn}(\Delta) \quad (38)$$

and

$$M = -\frac{H^{n+2} |W_{xx}|^{n-1} W_{xx}}{2(n+1)(n+2)} \left[(1+n-\check{\Xi})|1+\check{\Xi}|^{n+1} + (1+n+\check{\Xi})|1-\check{\Xi}|^{n+1} \right] - \frac{1}{2} BH^2 \text{sgn}(W_{xx})(1-\Xi^2), \quad (39)$$

where

$$\check{\Xi}(x, t) = \frac{2\Delta}{HW_{xx}}, \quad \Xi(x, t) = \text{Min}(1, |\check{\Xi}|). \quad (40)$$

Such a state requires $|\Sigma| > 2BH\Xi$ and $|M| > \frac{1}{2}BH^2(1-\Xi^2)$. On the other hand, if $|\Sigma| < 2BH\Xi$ and $|M| < \frac{1}{2}BH^2(1-\Xi^2)$, the fluid is rigid and $\Delta = W_{xx} = 0$. The variable Ξ represents the ratio of deformation in extension to that in bending, and exerts an important control on the integral contribution of the yield stress in (38) and (39).

Note that, as in the theory of perfectly plastic beams [10], the extensional stress in (36) is discontinuous across the “neutral curve”, $z - Z = \Delta/W_{xx}$. Such curves of discontinuity are a feature of ideal plasticity theory; fewer analogous results appear in the literature regarding the Herschel–Bulkley fluid, for which the regularity of the velocity field demanded by the viscous part of the stress tensor might further smooth the solution. If that were the case, the stress jump across $z - Z = \Delta/W_{xx}$ must be smoothed by a boundary layer, the details of which lie hidden at higher asymptotic orders. Although we ignore further discussion of this awkward point here, it is essential to point out that the stress jump in (36) divorces our model from that proposed in [5]. In that study, the stress field is assumed smooth and linear in z at the outset. The current analysis would suggest that this assumption is inconsistent with the Herschel–Bulkley constitutive model (which neglects elastic deformations, but which are included in [5]), given the leading-order form of the velocity field.

2.4. The Bingham catenary

We now discard surface tension ($\Gamma = 0$) and focus on a uniformly thick sheet ($H = 1$) of Bingham fluid ($n = 1$). The model derived above is then summarized as

$$Z_t = W, \quad \frac{\partial \Sigma}{\partial x} = 0, \quad \frac{\partial^2 M}{\partial x^2} + \Sigma Z_{xx} = G + \text{Re}W_t, \tag{41}$$

where

$$M = -\frac{1}{3}W_{xx} - \frac{1}{2}B(1 - \varepsilon^2)\text{sgn}(W_{xx}), \tag{42}$$

$$\Sigma = 4\Delta + 2B\varepsilon\text{sgn}(\Delta), \tag{43}$$

and

$$\Delta = U_x + Z_x W_x, \quad \varepsilon = \text{Min}\left(1, \left|\frac{2\Delta}{W_{xx}}\right|\right), \tag{44}$$

apply where the sheet is yielded. If the fluid is rigid, $W_{xx} = \Delta = 0$ and Σ and M are determined by (41), continuity, and the boundary conditions.

For the catenary, both ends of the sheet are fixed. These ends can be placed at $x = \pm 1$, given the freedom of the horizontal lengthscale \mathcal{L} in our non-dimensionalization. We then impose $W(\pm 1, t) = W_x(\pm 1, t) = U(\pm 1, t) = 0$. Similarly, we can exploit the freedom of the velocity scale U to set the parameter G to unity. We make this choice in all the calculations presented below, although we avoid explicitly putting $G = 1$ in the formulae since the effect of gravity is then made more transparent and because G remains a parameter in later sections where U is selected differently.

2.4.1. Small times

To begin, we ignore inertia, in which case two integrals of the second relation in (41) furnish

$$M = \Upsilon + \frac{1}{2}Gx^2 - \Sigma Z \tag{45}$$

(in view of the symmetry of the catenary about $x = 0$), where Υ is a constant of integration. For small times, Z is small, being $O(t)$. It is also not difficult to establish that Σ must also be of this order in this limit. Thus, (45) reduces to $M \approx \Upsilon + \frac{1}{2}Gx^2$, and in any yielded sections we have

$$M \approx -\frac{1}{3}W_{xx} - \frac{1}{2}B\text{sgn}(W_{xx}). \tag{46}$$

During the initial fall, the centre of the catenary is expected to attain the largest negative vertical velocity, whereas $W = W_x = 0$ at the fixed ends, reflecting local maxima in W . Thus, W_{xx} must vanish

somewhere between the centre and ends. As described in the previous subsection, such inflexions may herald the appearance of rigid plugs. It is therefore plausible to suppose that yielded zones appear over the central section of the catenary and at its edges, and allow for intervening rigid plugs.

Defining

$$x_a = \sqrt{-\frac{(2\Upsilon + B)}{G}} \quad \text{and} \quad x_b = \sqrt{\frac{(B - 2\Upsilon)}{G}}. \tag{47}$$

Eq. (46) gives

$$W_{xx} \approx \frac{3}{4}G \times \begin{cases} (x_a^2 - x^2), & |x| < x_a \\ (x_b^2 - x^2), & x_b < |x| < 1, \end{cases} \tag{48}$$

over the two yielded regions. The intervening plugs occupy $x_a < |x| < x_b$, where the sheet profile is linear in x . Thus, after matching W and W_x at the yield points, $x = \pm x_a$ and $\pm x_b$,

$$W \approx \begin{cases} W_0 - \frac{1}{8}Gx^2(x^2 - 6x_a^2), & |x| < x_a \\ W_0 + \frac{1}{8}Gx_a^3(8|x| - 3x_a), & x_a < |x| < x_b \\ \frac{1}{8}G(6x_b^2 - 2|x| - x^2 - 3)(1 - |x|)^2, & x_b < |x| < 1, \end{cases} \tag{49}$$

with

$$W_0 = -\frac{1}{8}G[8(1 - x_b)^3 - 5(1 - x_b)^4 + 8x_b^3x_b - 3x_b^4] \tag{50}$$

and

$$x_a^3 = \frac{1}{2}(1 - x_b)^2(2 + x_b). \tag{51}$$

Note that $W \rightarrow 0$, $\Upsilon \rightarrow -\frac{1}{2}B$, and $(x_a, x_b) \rightarrow (0, 1)$ for $B \rightarrow \frac{1}{2}G$. That is, the catenary becomes rigid throughout, so unless $B < \frac{1}{2}G$ the fluid does not deform at all (a criterion also derived in [5]). Also, the rigid plugs disappear if $x_a = x_b$. This corresponds to the Newtonian solution with $B = 0$ and $W = -G(1 - x^2)^2/8$. In other words, when B is decreased through $\frac{1}{2}G$, the catenary yields over narrow sections at the edges and centre; if B is lowered further to the Newtonian limit, the yielded zones expand and eventually merge together.

2.4.2. Later times

As the catenary falls with the fixed velocity structure in (49), Z grows linearly with time. Thus, for times of order unity, we can no longer neglect the term ΣZ in (45). We resort to numerical computations to determine the later-time evolution. For the task, we consider initial-value problems beginning with the initial conditions, $Z(x, 0) = 0$, $U(x, 0) = 0$ and $W(x, 0)$ given by (49).

To expedite the computations, we further introduce a number of modifications to the system defined by (41)–(44). First, we retain the inertial term in the third equation in (41) in order to preserve the form of that evolution equation. Moreover, we include an analogous term in the second of these equations: $\varepsilon^2 \text{Re}U_t = \Sigma_x$. This addition is not asymptotic, as it brings in only a single selection of the terms that arise at higher order of the expansion, but it modifies the equation so that it can also be time stepped. Provided $\varepsilon^2 \text{Re}$ and Re are sufficiently small, the system evolves such that Σ is practically independent of position and the vertical inertia is negligible (values less than about unity are found to be sufficient). Thus, we first modify the equations such that they constitute an initial-value problem for the dependent variables, $Z(x, t)$, $W(x, t)$ and $U(x, t)$.

Despite this reformulation, the transparency of the initial-value problem remains obscured by the yield condition and the need to apply different formulae over any rigid sections. Our second modification avoids this complication by regularizing the step functions in the definitions of M and Σ . Specifically, we replace $\text{sgn}(W_{xx})$ and

sgn(Δ) by $\tanh(f/\lambda)$, where $f = W_{xx}$ or Δ , and λ is a regularization parameter. This allows us to apply the constitutive law everywhere and avoid explicit consideration of the yield conditions, though at the expense of replacing the plugs with weakly yielded zones. We make λ as small as the computations will allow for given settings of B , Re and ϵ , and further decrease its size in time in order to avoid the regularization playing too significant a role in the evolution over long times when the catenary is settling into its final state (typical values of λ are 10^{-4} at the outset of the computation, and 10^{-5} by the end).

With these modifications, the two equations representing force balance are turned into standard partial differential evolution equations. We then evaluate spatial derivatives using Chebyshev collocation [16] and the resulting ordinary differential equations are integrated using a standard stiff time integrator (MATLAB's ODE15s), exploiting symmetry to compute only half of the catenary ($0 \leq x \leq 1$). Unfortunately, the code does not perform well with a fine spatial grid, and to allow for long time integrations, we were limited to resolutions of the order of 100 collocation points.

Sample solutions are shown in Figs. 3–5. The first of these figures displays snapshots of the deflection of the midline (i.e. $Z(x, t)$) for three representative values of B . The second figure displays the corresponding time series of $\Sigma(t)$, together with the locations of the rigid sections of the catenaries (i.e. the plugs, where $|M| < \frac{1}{2}B(1 - \Xi^2)$, shown shaded on a space–time diagram). The final figure displays snapshots of W , U and M .

For low values of yield stress (illustrated by the computation with $B = 0.1$ in Figs. 3 and 4), the catenary falls significantly and remains roughly parabolic, except near the ends. The stress resultant, $\Sigma(t)$, first climbs to a maximum before falling into a slow decline. Initially, two slender plugs are present, with borders predicted by the locations, $x = x_a$ and x_b , determined earlier. Somewhat later, however, these plugs shrink around two particular zero-crossings of M , which migrate towards the edges of the thread. At later times, further zero-crossings appear in more central areas, creating a complicated spatio-temporal pattern. As indicated in Fig. 5a, although M passes through zero, its magnitude does not apparently fall below $\frac{1}{2}B(1 - \Xi^2)$. Hence, for the lowest yield stresses, no localized plugs appear to survive the fall of the catenary.

For moderate yield stress ($B = 0.2$) the remnants of the two plugs present in the initial state play a more significant role, although they also thin slightly and migrate edgewards during the catenary's fall. In addition, a new plug region forms in the central section of the catenary for later times. Because both the older

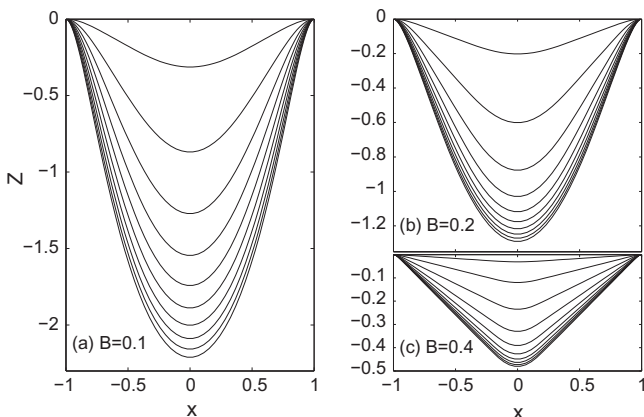


Fig. 3. Snapshots of falling catenaries for (a) $B = 0.1$, (b) $B = 0.2$ and (c) $B = 0.4$. The snapshots are shown for times of $t = 375\sqrt{j/10}$, $j = 1, 2, \dots, 10$.

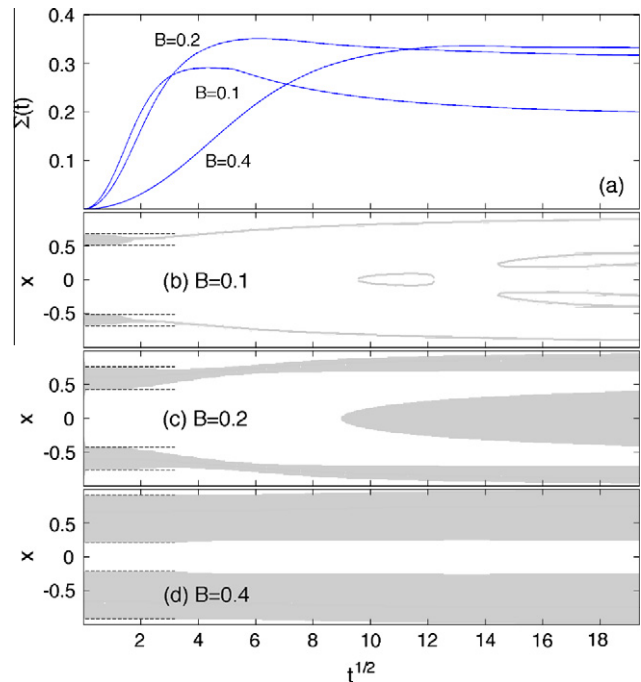


Fig. 4. Further details of the three computations of Fig. 3. In (a), $\Sigma(t)$ is plotted against $t^{1/2}$. Panels (b)–(d) show the locations of the plugs (as given by the regions where $|M| < \frac{1}{2}B(1 - \Xi^2)$). The dashed horizontal lines for $t^{1/2} < 3$ indicate $x = \pm x_a$ and $\pm x_b$ from (47) and (51). In (b), for the larger times, the grey lines track the loci of the positions where M switches sign.

plugs and the new one invade regions that were previously yielded, the catenary profile does not remain straight over these rigid sections. Instead, the sheet adopts a more complicated shape.

For the highest yield stress ($B = 0.4$), the two initial plugs remain intact and largely fixed in their original locations. The associated straight rigid sections of the catenary thereby persist throughout the evolution, and the fall is mediated by the yielded layers at the sheet's centre and edges. The shape consequently develops a distinctive triangular form with “plastic hinges” over those thin regions, much as noted in the dynamic loading of perfectly plastic beams ([8], chapter 7).

An important feature of the numerical solutions is that they suggest that the viscoplastic catenary does not fall indefinitely, unlike its viscous relative [15]. This is emphasized further in Fig. 6, which shows Σ and the greatest vertical extension of the catenary (i.e. $|Z(0, t)|$) as functions of time, for a wide range of yield stresses. In all the cases except those with small B , the vertical extension appears to slow and approach a constant value over large times. Continuing the integrations at small B yet further indicates that even these computations appear to converge towards steady states. Estimates of the final Σ and the distance that the catenary falls are included in Fig. 6.

Unfortunately, our numerical integrations are not particularly reliable over long times owing to the limitations of the numerical scheme and the regularization implicit in the code. Thus, it is difficult to be completely secure in the conclusion that the yield stress can halt the fall of the catenary, relying solely on these results. Instead, we now offer two asymptotic solutions that back up the conclusion. For yield stresses corresponding to order one Bingham numbers, Kamrin and Mahadevan [5] also arrive at this result, using their version of the slender-beam theory and a finite-element simulation of a two-dimensional elasto-plastic model. For $B = O(\epsilon)$, these authors show that the yield stress no longer arrests the fall of the catenary; in this regime, curvatures grow to order-one values, invalidating the theory of this section.

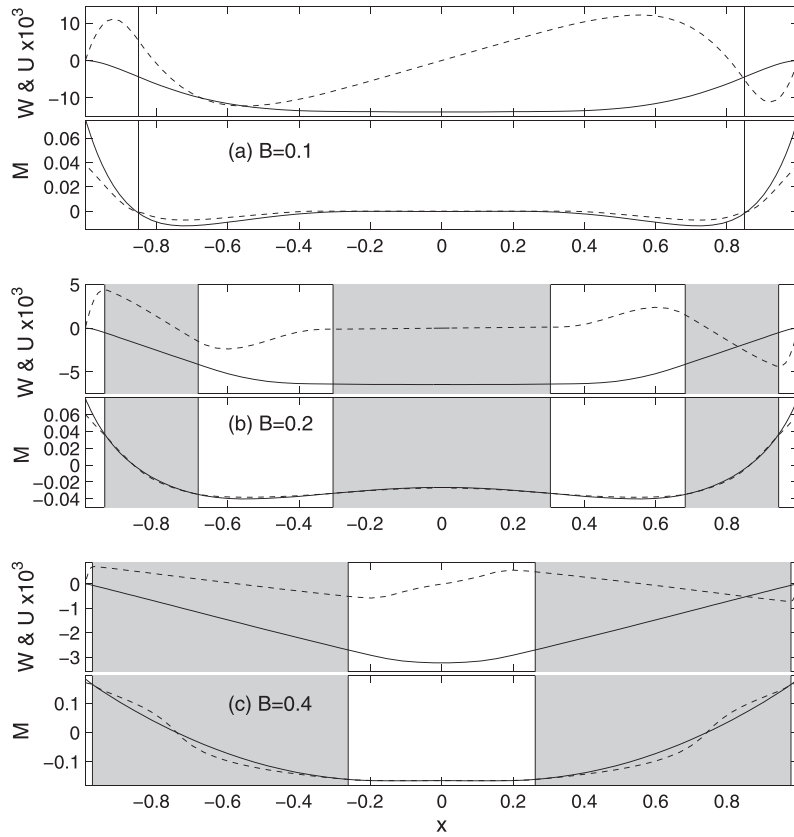


Fig. 5. More details of the three computations of Figs. 3 and 4. Panels (a)–(c) refer to the three values of B , with each panel showing snapshots at $t = 187$ of W (solid) and U (dashed) in the upper plots, and M (solid) and $-\frac{1}{2}B(1 - \varepsilon^2)\text{sgn}(W_{xx})$ (dashed) in the lower plots. The shaded regions in (b)–(c) are the plugs; the vertical lines in (a) indicate the zero-crossings of M .

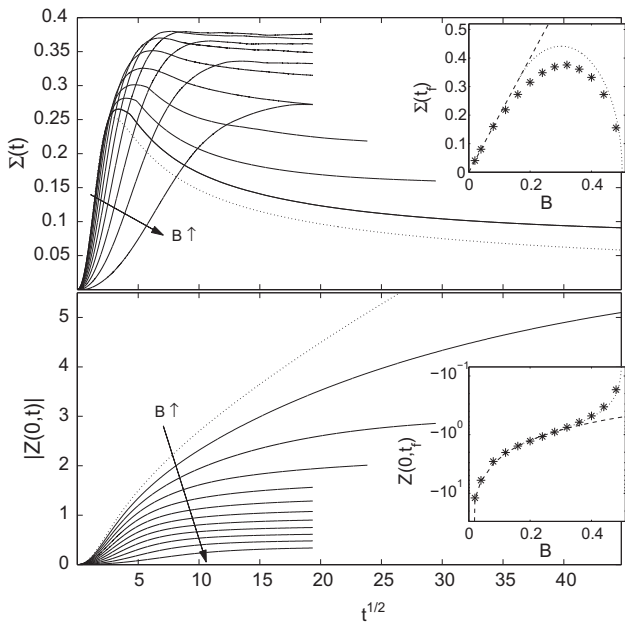


Fig. 6. Time series of (a) $\Sigma(t)$ and (b) $|Z(0,t)|$, for $B = 0.04, 0.08, \dots, 0.44$, with the trend of increasing yield stress indicated by the arrows. The dotted lines show the viscous case ($B = 0$). The insets show $|\Sigma(t_f)|$ and $|Z(0,t_f)|$ at the final time, $t = t_f$, of the computations (lasting longer than shown for the lower values of B); the dashed lines show the predictions from the separable solution in (52) and (57) and the dotted lines that in (67), (72) and (73).

2.4.3. Separable, low-yield-stress solutions

When there are no plugs within the catenary (which likely arises when B is small), we can search for a separable solution suitable once the vertical velocity W has declined sufficiently that the bending term M drops out of the main balance of forces. Then, $\Sigma Z \approx \gamma + \frac{1}{2}Gx^2$, or

$$Z \approx -\frac{G}{2\Sigma}(1 - x^2) \tag{52}$$

given that $Z(\pm 1, t) = 0$ (and that slender boundary layers exist at the ends over which the bending term returns to adjust the solution so that $W_x(\pm 1, t) = 0$). Hence,

$$W \approx \frac{G\dot{\Sigma}}{2\Sigma^2}(1 - x^2), \quad W_{xx} \approx -\frac{G\dot{\Sigma}}{\Sigma^2} \tag{53}$$

and

$$\Delta \approx U_x - 4x^2 \frac{G^2 \dot{\Sigma}}{\Sigma^3}. \tag{54}$$

Because W_{xx} is independent of x , it follows from (43) that Δ must also be independent of x , implying

$$U \approx -\frac{xG^2 \dot{\Sigma}}{3\Sigma^3}(1 - x^2). \tag{55}$$

Hence

$$\Sigma \approx -\frac{4G^2 \dot{\Sigma}}{3\Sigma^3} - 2B\text{sgn}(\dot{\Sigma})\text{Min}\left(1, \frac{2G}{3\Sigma}\right). \tag{56}$$

Regardless of the choice in $\text{Min}(1, 2G/3\Sigma)$, we find that $\dot{\Sigma} < 0$, and so (56) can be re-arranged into

$$\dot{\Sigma} \approx -\frac{\Sigma^2}{4G^2} \times \begin{cases} (3\Sigma^2 - 4BG), & 2G < 3\Sigma, \\ 3\Sigma(\Sigma - 2B), & 2G > 3\Sigma. \end{cases} \quad (57)$$

It follows that, for a finite yield stress, $\Sigma(t)$ converges to the limiting value, $\Sigma_\infty = \text{Min}(2B, \sqrt{4BG/3})$. Conversely, for $B = 0$, $\Sigma \sim t^{-1/3}$, as noted previously by Teichman and Mahadevan [15]. In other words, the yield stress arrests the fall of the catenary, as suggested by the numerical results.

Note that the numerical solutions presented earlier indicate that persistent plugs impede the convergence to a separable solution of this kind for $B \gtrsim 0.15$ with $G = 1$. Thus, the second limit, $\Sigma \rightarrow \sqrt{4BG/3}$, which occurs for $B > G/3$, is not relevant. A comparison of the separable solution with numerical computations at low B is presented in Fig. 7. The predictions for the final stress resultant ($\Sigma_\infty = 2B$) and furthest fall ($|Z(0, \infty)| = G/4B$) are also included in Fig. 6.

2.4.4. Catenaries featuring an undeformed pair of plugs

The numerical solutions suggest that when B is not far from its critical value ($0.36 \lesssim B < \frac{1}{2}, G = 1$), the paired plugs present in the initial condition remain largely intact throughout the evolution. These undeformed plugs border the yielded central section of the catenary, and are in turn buffered from the ends by two yielded boundary layers that become increasingly thin as time progresses (see Figs. 4c and 5c). Furthermore, we observe that the catenary approaches its final shape with U and W decreasing algebraically with time, $(U, W) \sim t^{-2}$ (see Fig. 8), and $\Xi < 1$. In this situation, we can again construct the final state analytically.

To describe the long-time dynamics, we set

$$Z = Z_0(x) + t^{-1}Z_1(x) + \dots, \quad (58)$$

$$W = t^{-2}W_2(x) + \dots, \quad U = t^{-2}U_2(x) + \dots, \quad (59)$$

$$\Sigma = \Sigma_0 + t^{-1}\Sigma_1 + \dots, \quad M = M_0(x) + t^{-1}M_1(x) + \dots, \quad (60)$$

and

$$\Xi = \Xi_0(x) + t^{-1}\Xi_1(x) + \dots, \quad (61)$$

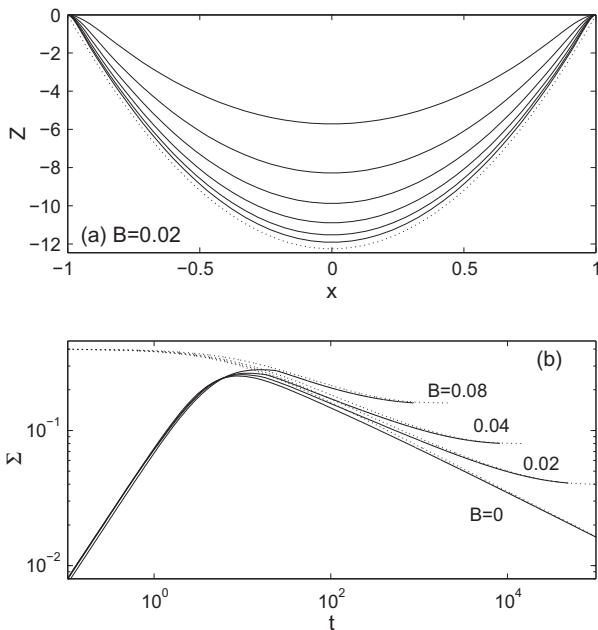


Fig. 7. Initial-value problems for small B . Panel (a) shows snapshots of $Z(x, t)$ with $B = 0.02$, at the times $t = 4.5 \times 10^4 \times \sqrt{j/6}, j = 1, 2, \dots, 6$. The dotted curve shows the separable solution in (52) with $\Sigma = 2B$. (b) shows Σ as a function of t for computations with the values of B indicated. The dotted lines are determined from integrating (57), assuming that $\Sigma(0) = 0.4$.

with $W_2 = -Z_1$. The inertialess force balance remains as in (45), with $\Upsilon = \Upsilon_0 + t^{-1}\Upsilon_1 + \dots$.

Within the yielded central section, the constitutive laws in (42) and (43) demand that

$$\Sigma_0 = 2B\Xi_0, \quad M_0 = -\frac{1}{2}B(1 - \Xi_0^2), \quad (62)$$

given that $\Xi_0 < 1$ and $W_{xx} > 0$ here. The following order of t^{-1} further indicates that $\Sigma_1 \propto \Xi_1$. Hence, both Ξ_0 and Ξ_1 are independent of position, which also indicates that M_0 and M_1 are likewise constant. Eq. (41) then implies that

$$Z_0 = Z_0(0) + \frac{Gx^2}{2\Sigma_0} \quad \text{and} \quad Z_{1x} = -\frac{xG\Sigma_1}{\Sigma_0^2}. \quad (63)$$

If the plugs are largely undeformed, then Z and W must be linear functions of position there. Moreover, in the late-time limit, when the boundary layers at the edges are sufficiently thin, $Z_0 \rightarrow 0$ for $|x| \rightarrow 1$. Thus, on demanding that Z_0, M_0 and their first derivatives match with the solution for the yielded midsection, we find

$$Z_0 = \begin{cases} G(x_a^2 - 2x_a + x^2)/2\Sigma_0, \\ Gx_a(|x| - 1)/\Sigma_0, \\ |x| < x_a \quad \text{and} \quad x_a < |x| < 1, \end{cases} \quad (64)$$

$$M_0 = \begin{cases} -\frac{1}{2}B(1 - \Xi_0^2), \\ -\frac{1}{2}B(1 - \Xi_0^2) + \frac{1}{2}G(|x| - x_a)^2, \\ |x| < x_a \quad \text{and} \quad x_a < |x| < 1, \end{cases} \quad (65)$$

As the plug solution limits to the boundary layers at the edge, on the other hand, $M_0 \rightarrow +\frac{1}{2}B(1 - \Xi_0^2)$, in view of the reversal of the sign of W_{xx} . Hence,

$$x_a = 1 - \sqrt{\frac{2B}{G}(1 - \Xi_0^2)}. \quad (66)$$

Note that the furthest fall of the catenary is therefore given by

$$|Z_0(0)| = \frac{Gx_a(2 - x_a)}{2\Sigma_0}. \quad (67)$$

To determine Σ_0 (or Ξ_0), we need to study U_2 : over the central yielded section, from (44) and (62), we have

$$U_{2x} = Z_{0x}Z_{1x} - \frac{1}{2}\Xi_0Z_{1xx} \rightarrow \frac{G\Sigma_1\Xi_0}{2\Sigma_0^2} - \frac{x^2G^2\Sigma_1}{\Sigma_0^3}. \quad (68)$$

But over the plugs, where $\Delta = 0$ and matching requires

$$W_{2x} = -Z_{1x} = \frac{x_aG\Sigma_1}{\Sigma_0^2}, \quad (69)$$

we find

$$U_{2x} = -\frac{x_a^2G^2\Sigma_1}{\Sigma_0^3}. \quad (70)$$

These relations can be integrated from $x = 0$, where $U_2 = 0$, up to the boundary layers at the edges, where U_2 must match onto the corresponding boundary-layer solution. For the latter, we argue that, since Z_x and W_x must both become small in order to satisfy the boundary conditions, then $U_x \sim -\Sigma_0 W_{xx}/4B$ in the boundary layers (given that $W_{xx} < 0$ and $\Sigma \sim -2B\Xi$ there). Hence, integrating over the boundary layer, we find the matching condition,

$$U_2 = -\frac{\Sigma_0 W_{2x}}{4B} = -\frac{Gx_a\Sigma_1}{4\Sigma_0 B}, \quad \text{for } x \rightarrow \pm 1. \quad (71)$$

After sorting through the remaining algebraic details, we arrive at

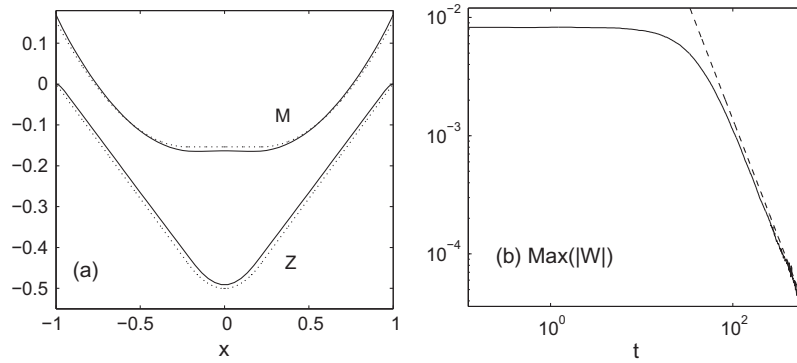


Fig. 8. Final solution of a computation with $B = 0.4$. Panel (a) shows Z and M . The dotted lines are the predictions from (64) and (65). In (b), the time series of the minimum values of $W(x, t)$ is shown, along with the trend, t^{-2} .

$$\Sigma_0 = \sqrt{\frac{2\chi_a BG}{3}(3 - 2\chi_a)}, \tag{72}$$

which, from (66), further implies

$$\chi_a = \frac{1}{2} \left[3 - \sqrt{3 \left(\frac{8B}{G} - 1 \right)} \right]. \tag{73}$$

The predictions from (65), (72) and (73) are compared with numerical results in Figs. 6 and 8. The asymptotic solutions for Σ_0 and $|Z_0(0)|$ end at $B = G/6$ when $\chi_a \rightarrow 1$, corresponding to an intersection with the curves given by the theory for low B derived earlier. However, a central plug forms in the initial-value problems with $0.15 \lesssim B \lesssim 0.36$ and $G = 1$, invalidating both theories before they intersect.

Note that it is not possible to perform a complementary analysis to provide the final state for arbitrary B because of the dynamics of the plug regions: these regions can migrate, appear or disappear during the catenary’s evolution. Consequently, the rigid zones are not necessarily straight, but have a shape dictated by the history of the falling catenary; without analytical solutions like those in (64) we cannot connect the solution for the yielded sections to the boundary layers.

3. Order-one curvature

3.1. Dimensional formulation

We next consider a thin sheet that is bent sufficiently that curvatures become order one. As sketched in Fig. 2, the sheet is now described by a coordinate system, (s, n) , based on arc-length s and the normal coordinate n . With respect to the Cartesian coordinates of Section 2, a point on the midline is described by the vector $\mathbf{r}_c(s, t)$, and the local curvilinear coordinate axes make an angle $\theta(s, t)$ with the horizontal. Adjusting the notation from Section 2, we now define $\mathbf{u} = (u, w)$ as the velocity in the *curvilinear* coordinate system (with respect to the (s, n) axes). Similarly, the stress tensors, τ_{ij} and σ_{ij} , are also now referred to this system. To ease the construction of the model, we ignore both inertia and surface tension, and adopt the Bingham model.

In the curvilinear coordinate system, conservation of mass and force balance can be expressed in the form [3,11]

$$\frac{\partial u}{\partial s} + h \frac{\partial w}{\partial n} - \kappa w = 0, \tag{74}$$

$$\frac{\partial \sigma_{ss}}{\partial s} + h \frac{\partial \sigma_{sn}}{\partial n} - 2\kappa \sigma_{sn} = \rho gh \sin \theta, \tag{75}$$

$$\frac{\partial \sigma_{sn}}{\partial s} + h \frac{\partial \sigma_{nn}}{\partial n} + \kappa(\sigma_{ss} - \sigma_{nn}) = \rho gh \cos \theta, \tag{76}$$

where

$$\kappa \equiv \frac{\partial \theta}{\partial s} \quad \text{and} \quad h \equiv 1 - \kappa n, \tag{77}$$

denote the curvature and metric coefficient.

The upper and lower surfaces of the sheet are located at $n = \pm \frac{1}{2} H(s, t)$. Here, force balance and the kinematic conditions demand that

$$h \sigma_{sn} \mp \frac{1}{2} \sigma_{ss} \frac{\partial H}{\partial s} = h \sigma_{nn} \mp \frac{1}{2} \sigma_{sn} \frac{\partial H}{\partial s} = 0, \tag{78}$$

and

$$w = w_c \pm \frac{1}{2} \left[\frac{\partial H}{\partial t} + \frac{1}{h} \left(u - u_c \pm \frac{1}{2} H \frac{\partial \theta}{\partial t} \right) \frac{\partial H}{\partial s} \right], \tag{79}$$

where $\mathbf{u}_c = (u_c, w_c)$ denotes the velocity of the centreline of the sheet. The expression in (79) results from the fact that $n = \pm \frac{1}{2} H$ denote material surfaces, and the material derivative relevant for the current coordinate system is

$$\frac{D}{Dt} = \frac{\partial}{\partial t} + \frac{1}{h} \left(u - u_c + n \frac{\partial \theta}{\partial t} \right) \frac{\partial}{\partial s} + (w - w_c) \frac{\partial}{\partial n}.$$

Note that $\hat{\mathbf{s}} = \partial \mathbf{r}_c / \partial s \equiv (\cos \theta, \sin \theta)$ and $\mathbf{u}_c = \partial \mathbf{r}_c / \partial t$, and so

$$\frac{\partial \theta}{\partial t} = \frac{\partial w_c}{\partial s} + \kappa u_c \quad \text{and} \quad \frac{\partial u_c}{\partial s} = \kappa w_c. \tag{80}$$

3.2. Scaling and the approximate velocity field

As in the small-curvature theory, we use a characteristic thickness, \mathcal{H} , length, \mathcal{L} , speed, \mathcal{U} , and stress, \mathcal{S} , to non-dimensionalize the variables:

$$\hat{s} = \frac{s}{\mathcal{L}}, \quad (\hat{n}, \hat{H}) = \frac{1}{\mathcal{H}} (n, H), \quad (\hat{u}, \hat{w}) = \frac{1}{\mathcal{U}} (u, w), \tag{81}$$

with $\hat{t} = \mathcal{L}^{-1} \mathcal{U} t$, and

$$\hat{\tau}_{ij} = \frac{\tau_{ij}}{\mathcal{S}}, \quad (\hat{\sigma}_{ss}, \epsilon \hat{\sigma}_{sn}, \epsilon \hat{\sigma}_{nn}) = \frac{1}{\mathcal{S}} (\sigma_{ss}, \sigma_{sn}, \sigma_{nn}). \tag{82}$$

This scaling is guided by the form of (75) and (76). Note that the velocity component, u , and the extensional stress component, σ_{nn} , are now one order larger than in the previous section, as is the time scale.

With these rescalings, and after dropping the hat decoration, conservation of mass becomes

$$\epsilon \frac{\partial u}{\partial s} + (1 - \epsilon \kappa n) \frac{\partial w}{\partial n} - \epsilon \kappa w = 0. \tag{83}$$

Moreover, on scaling the rate-of-strain tensor with $\epsilon \mathcal{U} / \mathcal{L}$, the dimensionless constitutive law is

$$\tau_{ij} = \dot{\gamma}_{ij} + B\dot{\gamma}_{ij}/\dot{\gamma}, \quad \text{if } \tau = \sqrt{\tau_{ss}^2 + \tau_{sn}^2} > B, \quad (84)$$

and $\dot{\gamma}_{ij} = 0$ otherwise, where

$$\dot{\gamma}_{ss} = \frac{2}{\epsilon} \frac{(\partial u/\partial s - \kappa w)}{(1 - \epsilon\kappa n)}, \quad \dot{\gamma}_{nn} = \frac{2}{\epsilon} \frac{\partial w}{\partial n},$$

$$\dot{\gamma}_{sn} = \frac{1}{\epsilon} \frac{(\partial w/\partial s + \kappa u)}{(1 - \epsilon\kappa n)} + \frac{1}{\epsilon^2} \frac{\partial u}{\partial n}. \quad (85)$$

In view of the scaling of the total stress components in (82), which imply that the dimensionless pressure is $p = -\frac{1}{2}(\sigma_{ss} + \epsilon\sigma_{nn})$, the deviatoric stresses are given to leading order by

$$\tau_{ss} = \sigma_{ss} + p = \frac{1}{2}\sigma_{ss}, \quad \tau_{sn} = \epsilon\sigma_{sn}, \quad \tau_{nn} = -\tau_{ss}. \quad (86)$$

Thus, τ_{ss} and τ_{nn} are order one, but τ_{sn} must be order ϵ . In turn, from the constitutive law, this demands that $(\dot{\gamma}_{ss}, \dot{\gamma}_{nn}) \sim O(1)$ and $\dot{\gamma}_{sn} \sim O(\epsilon)$, despite the expressions in (85), which contain additional factors of ϵ^{-1} . To avoid this inconsistency, we must carefully choose the leading-order form of the velocity field. From the physical perspective, this is equivalent to observing that, in order to preserve the slender geometry of the sheet, the velocity field must have a specific dependence on the transverse coordinate n . This dependence is the same as for a Newtonian sheet [11].

More specifically, the conservation of mass equation and the scalings for the deviatoric stresses can be satisfied if the velocity field takes the form,

$$w = W(s, t) + O(\epsilon^2), \quad u = U(s, t) - \epsilon(W_s + \kappa U)n + O(\epsilon^2), \quad (87)$$

where

$$U_s - \kappa W = O(\epsilon). \quad (88)$$

If we define

$$\Delta = \epsilon^{-1}(U_s - \kappa W) \quad \text{and} \quad \Omega = (W_s + \kappa U)_s \quad (89)$$

as the stretching and bending rates of the centreline [11], we then have

$$\dot{\gamma}_{ss} = 2\Delta - 2\Omega n + O(\epsilon), \quad \dot{\gamma} = |\dot{\gamma}_{ss}| + O(\epsilon^2) \quad (90)$$

$$\sigma_{ss} = 4\Delta - 4\Omega n + 2B\text{sgn}(\Delta - \Omega n) + O(\epsilon). \quad (91)$$

3.3. Reduction

As in the small curvature case, the strain rate $\dot{\gamma}_{ss}$ changes sign at $n = \Delta/\Omega$, and we define

$$\Xi = \text{Min}\left(1, \left|\frac{2\Delta}{H\Omega}\right|\right), \quad (92)$$

(cf. (44)). The resultant extensional stress and bending moment, in the case that the fluid is yielded, are then

$$\Sigma = \int_{-\frac{1}{2}H}^{\frac{1}{2}H} \sigma_{ss} dn = 4H\Delta + 2BH\Xi\text{sgn}(\Delta) + O(\epsilon), \quad (93)$$

and

$$M = \int_{-\frac{1}{2}H}^{\frac{1}{2}H} n\sigma_{ss} dn - \frac{1}{3}H^3\Omega - \frac{1}{2}BH^2(1 - \Xi^2)\text{sgn}(\Omega) + O(\epsilon). \quad (94)$$

As in the small curvature theory, we may formulate integral expressions of force balance by integrating Eqs. (75) and (76) over n . Similarly, an expression of torque balance follows from integrating the product of (76) and n . In dimensionless form and ignoring small terms of $O(\epsilon^2)$, the result is

$$\frac{\partial \Sigma}{\partial s} - \epsilon\kappa M = \epsilon GH \sin \theta, \quad (95)$$

$$\epsilon \frac{\partial^2 M}{\partial s^2} + \kappa \Sigma = \epsilon GH \cos \theta, \quad (96)$$

where as before, $G = \rho g H / \epsilon^2 S$. When $\kappa = O(\epsilon)$, these relations reduce to (27) and (32) at leading order. Now, with $\kappa = O(1)$, the leading order form requires $\Sigma = O(\epsilon)$. Hence we write

$$\Sigma = \epsilon N, \quad (97)$$

and

$$\frac{\partial N}{\partial s} - \kappa M = GH \sin \theta, \quad (98)$$

$$\frac{\partial^2 M}{\partial s^2} + \kappa N = GH \cos \theta. \quad (99)$$

Re-examining (93), the stress condition $\Sigma = O(\epsilon)$ implies that $\Xi = O(\epsilon)$ and $\Delta = O(\epsilon)$ so that the sheet stretches only at $O(\epsilon^2)$. As in the Newtonian case, stretching is less significant than in the small curvature limit since the large curvature allows the sheet to deform by bending instead [3,4]. Thus the expression in (94) may be simplified to

$$M = -\frac{1}{3}H^3\Omega - \frac{1}{2}BH^2\text{sgn}(\Omega), \quad \text{if } |\Omega| > \frac{1}{2}BH^2; \quad (100)$$

otherwise $\Omega = 0$ and the sheet is rigid. Note that to relate N to the stretching of the sheet, the full complement of $O(\epsilon)$ corrections must be included in σ_{ss} and (93). This is not required for our current purposes; the details are, however, provided in the next section where they feature in the combined theory summarized there.

Finally, substitution of the velocity field (87) into the kinematic conditions in (79) and (80) now indicates that $w_c \sim W + O(\epsilon^2)$ and

$$\frac{\partial H}{\partial t} + \bar{U} \frac{\partial H}{\partial s} = O(\epsilon^2), \quad (101)$$

while

$$\frac{\partial \theta}{\partial t} + \bar{U} \frac{\partial \theta}{\partial s} = \frac{\partial W}{\partial s} + \kappa U + O(\epsilon^2). \quad (102)$$

Here, $\bar{U} = U - u_c$ is the translation speed of the fluid with respect to the centreline, which is independent of s to $O(\epsilon^2)$, and equal to a prescribed extrusion speed, $\bar{U} = U_e(t)$, if fluid is fed into the sheet from one end. Eq. (101) indicates that, to leading order, the sheet thickness again does not change, and we may take $H = 1$ for a sheet with uniform initial or extruded thickness.

In summary, the reduced model for the sheet with order one curvature is given by (98) and (99), with θ evolving according to (102); where fluid is yielded, M is related to Ω by (100). Provided the boundary conditions determine the stresses at one end (as in the free-end problems described below), the resultant stress N is furnished by integrating (98) without any need to employ the constitutive law to relate this quantity to the stretching rate.

3.4. The viscoplastic version of Galileo's problem

We now illustrate the order-one curvature theory with two model problems. In the first, we examine the deflection of an initially horizontal beam with one end fixed and the other free. This is the viscoplastic counterpart of the elastic problem posed centuries ago by Galileo.

We locate the fixed end at $s = 0$ and the free end at $s = L$. At the fixed end, we have

$$U(0, t) = W(0, t) = W_s(0, t) = \theta(0, t) = 0. \quad (103)$$

The stress-free conditions at the free end, $\sigma_{xz} = \sigma_{xx} = 0$, imply that

$$N(L, t) = M(L, t) = M_s(L, t) = 0. \quad (104)$$

Note that the dimensionless parameters, L and G , can be chosen as unity, in view of the freedom in the characteristic length, \mathcal{L} , and speed, \mathcal{U} .

3.4.1. Small displacements

At small times, θ and κ are also small, and the bending moment follows from integrating (99) subject to (104):

$$M \approx \frac{1}{2}G(L-s)^2 \tag{105}$$

(taking $H = 1$). The constitutive expression (100) for M implies that the fluid is rigid with $0 = \Omega \approx W_{ss}$ if $M < \frac{1}{2}B$. Thus, when

$$L < L_c \equiv \sqrt{\frac{B}{G}} \tag{106}$$

the moment is not sufficient for the beam to yield anywhere, and so there is no deflection. If $L > L_c$, on the other hand, only the section $L - L_c < s < L$ remains rigid, and the beam bends over the interval $0 < s < L - L_c$, such that

$$\frac{1}{3}W_{ss} \approx -\text{sgn}(M) \left(|M| - \frac{1}{2}B \right) = -\frac{1}{2}G \left[(L-s)^2 - L_c^2 \right]. \tag{107}$$

Thus, using the boundary conditions (103),

$$W \approx -G \left[\frac{1}{8}(L-s)^4 - \frac{1}{8}L^4 - \frac{3}{4}L_c^2s^2 + \frac{1}{2}L^3s \right], \tag{108}$$

for $0 < s < L - L_c$, and

$$W \approx -G \left[\frac{1}{8}(L^4 - L_c^4) - \frac{3}{4}L_c^2(L^2 - L_c^2) - \frac{1}{3}L_c^3(L - L_c) + \left(L_c^3 - \frac{3}{2}L_c^2L + \frac{1}{2}L^3 \right) s \right] \tag{109}$$

for $L - L_c < s \leq L$.

For small deflections, the centreline position is approximately $z = Z(s, t)$ (as in Section 2) with $\theta = Z_s$, and (102) reduces to the familiar equation, $Z_t = W$. Thus, since W is a prescribed function of position, the deflection grows linearly with time until the small displacement approximation becomes invalid.

3.4.2. Large displacements

For later times we resort to numerical solution of the $O(1)$ curvature Eqs. (98)–(102). We discretize (98) and (99) using first-order finite differences on a uniform grid, incorporating the stress boundary conditions (104). Having thus calculated $M(s, t)$, and hence $\Omega(s, t)$ from (100), Eq. (89) is similarly discretized, incorporating the boundary conditions (103), to calculate U and W . Eq. (102) can then be integrated in time to determine $\theta(s, t)$, from which we can reconstruct $\mathbf{r}_c(s, t)$:

$$\mathbf{r}_c(s, t) = \int_0^s (\cos \theta, \sin \theta) ds. \tag{110}$$

Note that this construction does not require us to regularize the constitutive law, unlike our scheme for the catenary in Section 2.4.

Snapshots of sagging beams for three values of B are shown in Fig. 9, and compared with the small displacement solution from (108) and (109). The unyielded sections of the sheet are shown by grey lines, while the yielded region is shown by a black line. The low-yield-stress solution with $B = 0.01$ in the first panel is very similar to the corresponding Newtonian solution [11], except for a small solid plug adjacent to the free end. The beam sags more slowly and the rigid sections are wider for the higher yield stresses. Importantly, as these beams fall downwards and rotate towards the vertical, the gravitational moment decreases below that given by (105). More of the beam then freezes into place, forming bent rigid sections. Eventually, the beam converges to a steady state with $M < \frac{1}{2}B$ everywhere.

The final shape of the beam is therefore controlled by the time-dependent expansion of the plugs, preventing us from providing

any analytical solutions for general B . Nevertheless, when B is close to GL^2 an approximate solution can be derived. In this limit, only a small region close to $s = 0$ yields and bends; the bulk of the beam remains rigid and straight, hinging with an angle $\theta = \Theta(t)$ on the boundary layer at the fixed end (cf. the solution with $B = 0.9$ and $GL^2 = 1$ in panel (c) of Fig. 9). For the rigid section, $\kappa = 0$ and so (99) gives $M = \frac{1}{2}G(L-s)^2 \cos \Theta$. The fluid therefore yields at $s = L - (B/G \cos \Theta)^{1/2} \ll L$ (where $|M| \rightarrow \frac{1}{2}B$). As the rigid section rotates, this yield point moves back to $s = 0$, whereupon the beam comes to rest with

$$\Theta = \cos^{-1}(B/GL^2). \tag{111}$$

This prediction is compared with the numerical solution for $B = 0.9$ in Fig. 9.

3.5. The extruded beam

Our second example is the viscoplastic analogue of Ribe's [11] subducting slabs: the beam is extruded through a fixed end at $s = 0$ with a prescribed speed and angle:

$$U(0, t) = U_e, \quad W(0, t) = W_s(0, t) = 0, \quad \theta(0, t) = \theta_e. \tag{112}$$

For illustration, we take $\theta_e = 0$, and by choice of velocity scale we set $U_e = 1$. Because the fluid undergoes very little extension, the beam lengthens at the extrusion speed, and so the free end is located at

$$s = L(t) = L_0 + U_e t, \tag{113}$$

where L_0 is the initial length. Once more, we impose

$$N(L, t) = M(L, t) = M_s(L, t) = 0. \tag{114}$$

3.5.1. Small displacements

When displacements are small, the solution derived for W in Section 3.4.1 applies equally to the extruded beam. The only difference is that L , and hence W , now vary with time, and, because the extrusion is not necessarily horizontal, we must replace G by $G \cos \theta_e$ to account for the inclination of gravity. Eq. (102) becomes

$$Z_t + U_e Z_s = W, \tag{115}$$

which can be integrated analytically given the solution for W in Section 3.4.1.

The small-time solution indicates that the extrusion begins with a rigid plug of length $L(t) < L_c$ being pushed out of the fixed end.¹ Once $L(t)$ surpasses L_c , the gravitational moment exceeds $\frac{1}{2}B$ at $s = 0$, creating an expanding yielded zone over which the beam bends downwards. Again, when the beam droops sufficiently to effectively reduce the gravitational moment, the small displacement approximation becomes invalid.

3.5.2. Larger displacements

To compute solutions for larger displacements we use the same numerical procedure as in Section 3.4.2, except that we employ a spatial grid that translates with the extrusion speed; new grid points are continually added to the solution domain at $s = 0$ to account for the extrusion of fresh fluid. Sample solutions with different yield stress are shown in Figs. 10 and 11. As predicted by the small-time solution, the fluid yields near the extrusion when the critical length, $L_c = \sqrt{B/G}$, is exceeded. Thereafter, the beam bends distinctively around on itself, curling underneath the extrusion and

¹ We ignore how the fluid is extruded, such as from the tube in Fig. 1. In fact, in order to be pushed through the tube, the fluid may be forced to yield and cannot therefore emerge as a plug. Instead, the fluid adjusts towards the rigid state over a small exit region, the description of which lies beyond our slender approximation.

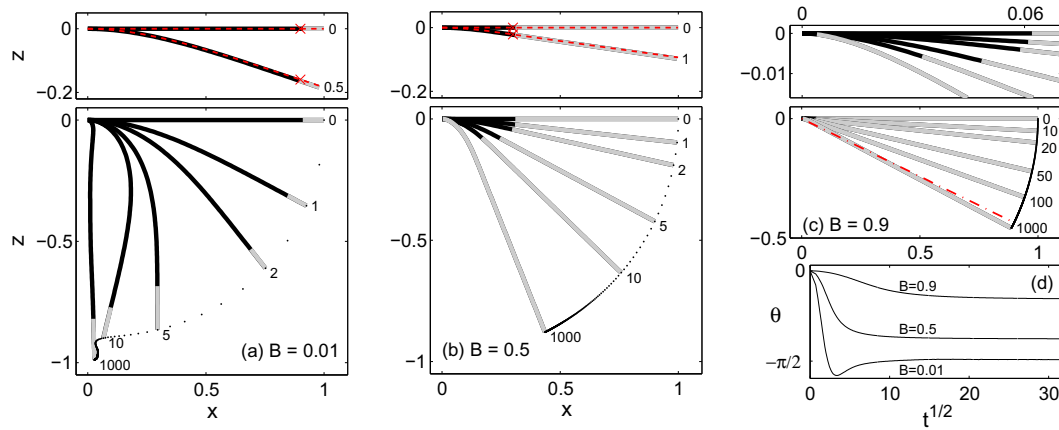


Fig. 9. (a)–(c) Snapshots of sagging beams at the times indicated for (a) $B = 0.01$, (b) $B = 0.5$ and (c) $B = 0.9$, with $G = 1$, $L = 1$ and $\theta(s, 0) = 0$. Black lines indicate the yielded sections, whereas the grey lines represent unyielded plugs; the dots show the path of the free end (plotted every 0.5 time units). For panels (a) and (b), the plots immediately above compare two snapshots with the corresponding small displacement approximation of Section 3.4.1 (dashed lines, with the yield point $s = L - L_c$ indicated by the cross). The upper panel for (c) shows a magnification of the yielded hinge near the fixed end. The dot-dashed line in (c) shows the $B \sim GL^2$ approximation given by (111). Panel (d) shows the angle of the free end as a function of \sqrt{t} for the three computations.

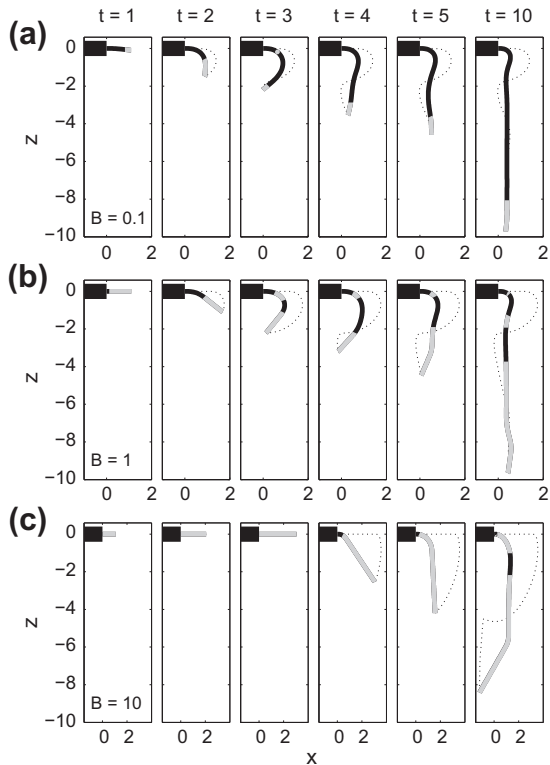


Fig. 10. Snapshots of extruded beams for the values of B indicated, $U_e = G = 1$, $\theta_e = 0$ and $L_0 = 0.1$. Black sections are yielded, grey sections denote plugs, and the dotted lines show the path of the free end.

finally collapsing towards the vertical.

Notable features of the solutions are the ‘kinks’ that become frozen into the shape of the beam, particularly near the free end. These kinks emerge when the gravitational moment, $|M|$, acting on previously yielded sections declines below $\frac{1}{2}B$, once those sections bend and rotate underneath the point of extrusion. This effect is countered by the continued horizontal extrusion which builds the moment back up, and by the swinging of the free end to positions to the left of the extrusion point, which generates negative

moments. The result is a relatively complicated spatio-temporal pattern of intertwined plugs and yielded regions, as seen in panel (c) of Fig. 11.

4. A higher-order model

The models presented above are complementary, but different versions of slender sheet theory for a viscoplastic fluid. In particular, if one adopts the second model, and then takes the limit that the curvature becomes small, one only recovers the small-curvature theory if, in that theory, the stretching rate, Δ , vanishes to leading order (compare (42) and (100); if $\Delta \rightarrow 0$, then $\mathcal{E} \rightarrow 0$ and the two formulae coincide). The key point is that the degree of curvature exerts a critical control on the extensional stresses and rate of stretching within the sheet *via* the main balance of forces: when the curvature is relatively small, higher extensional stresses are permitted in comparison to bending forces, allowing for greater stretching rates. With order-one curvatures, however, the bending stresses can only balance much lower extensional stresses, and the corresponding stretching rates are necessarily smaller. These physical ingredients are incorporated using different asymptotic scalings in the two models (in the small curvature model, $\int \sigma_{xx} dz = \Sigma$, whereas the order-one curvature theory takes $\int \sigma_{ss} dn = \epsilon N$).

To avoid an unsatisfying division of the dynamical behaviour into two different models we must therefore mix the asymptotic orderings. In particular, the key is to proceed to higher order in the order-one curvature theory and retain the next-order terms. Important milestones of this construction are relegated to Appendix A, as it amounts to a longer-winded version of the derivation of Section 3. Here, we simply quote the combined, higher-order formulation that results, and apply this theory to the problem of the Euler buckling of a viscoplastic column.

Without surface tension and inertia, the equations of force balance remain

$$\frac{\partial \Sigma}{\partial s} - \epsilon \kappa M = \epsilon GH \sin \theta, \tag{116}$$

$$\epsilon \frac{\partial^2 M}{\partial s^2} + \kappa \Sigma = \epsilon GH \cos \theta. \tag{117}$$

The sheet thickness and inclination evolve according to

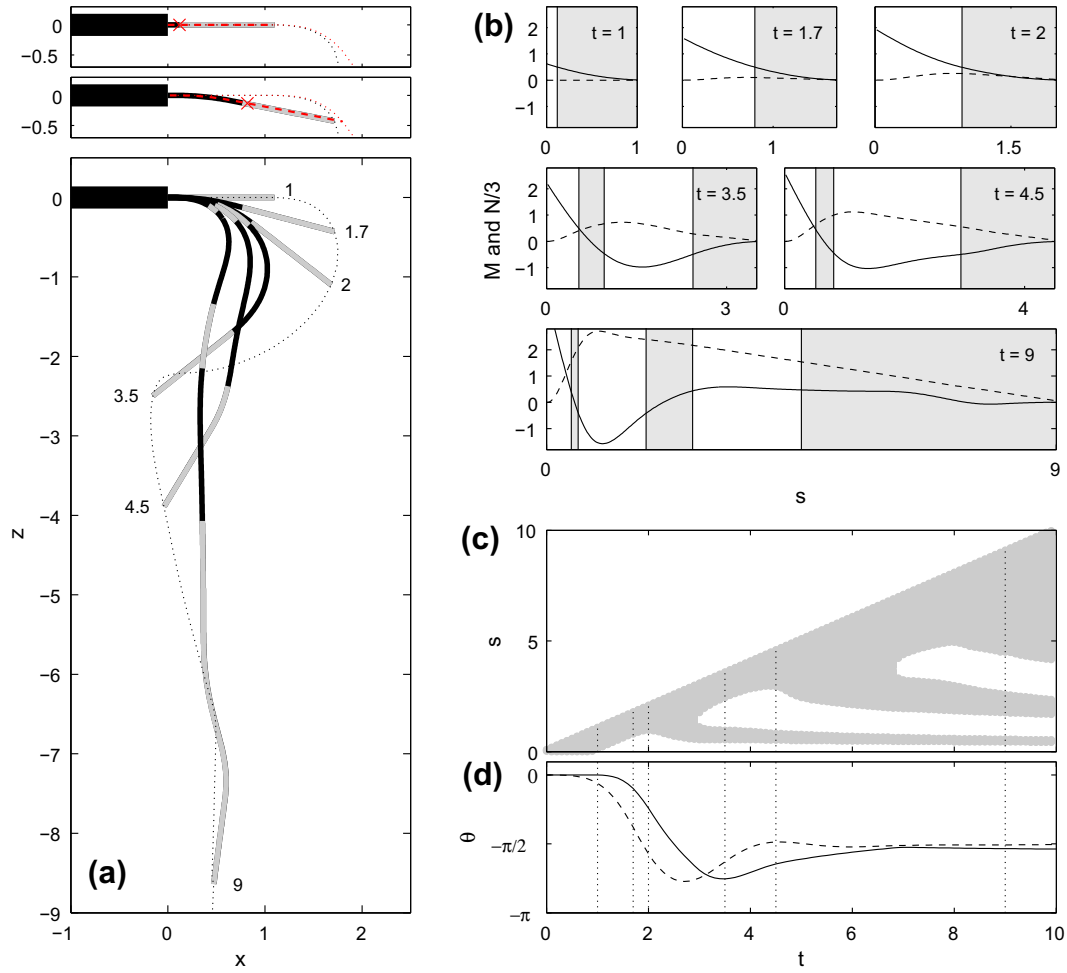


Fig. 11. (a) Snapshots at the times indicated of the extruded beam with $B = 1$; black and grey shading distinguishes the yielded sections and plugs, respectively, and the dotted line shows the path taken by the free end. The upper plots compare the solution at the first two times with the small-displacement solution of Section (3.5.1) (dashed line, with the yield point indicated by the cross; the right-most dotted lines also correspond to this small-displacement solution). (b) Bending moment M (solid) and scaled extensional stress $N/3$ (dashed), as functions of arc length s , for the times shown in (a). The plugs (with $|M| < \frac{1}{2}B$) are shown shaded. (c) Space–time diagram of the evolution of the plugs (shaded). (d) Time series of the angle at the free end, with the dashed line showing the equivalent Newtonian solution. The vertical dotted lines in (c) and (d) indicates the times of the snapshots shown in (a) and (b). $U_e = G = 1$, $\theta_e = 0$ and $L_0 = 0.1$.

$$\frac{\partial H}{\partial t} + \frac{\partial}{\partial s}(H\bar{U}) = 0, \quad \frac{\partial \bar{U}}{\partial s} = \frac{\partial U}{\partial s} - \kappa W, \quad (118)$$

$$\frac{\partial \theta}{\partial t} + \bar{U} \frac{\partial \theta}{\partial s} = \frac{\partial W}{\partial s} + \kappa U. \quad (119)$$

Where the fluid is yielded, the constitutive law demands

$$\Sigma = 4H\Delta + 2BH\varepsilon \text{sgn}(\Delta) - \frac{5}{6}\epsilon\kappa H^3\Omega - \frac{1}{2}\epsilon\kappa BH^2(1 - \varepsilon^2)\text{sgn}(\Omega), \quad (120)$$

$$M = -\frac{1}{3}H^3\Omega - \frac{1}{2}BH^2(1 - \varepsilon^2)\text{sgn}(\Omega). \quad (121)$$

Here, as in Section 3,

$$\Delta = \frac{U_s - \kappa W}{\epsilon}, \quad \Omega = (W_s + \kappa U)_s, \quad \varepsilon = \text{Min}\left(1, \left|\frac{2\Delta}{H\Omega}\right|\right).$$

Alternatively, if the fluid is rigid, $\Delta = \Omega = 0$.

4.1. Yield conditions

Fluid first yields when the extensional stress and moment exceed a threshold determined by the constitutive relations in (120) and (121). Those relations may be re-organized into the inequalities,

$$\left| \Sigma - \epsilon\kappa M + \frac{1}{2}H^2\Omega \right| \geq 2BH\varepsilon \quad (122)$$

and

$$|M| \geq \frac{1}{2}BH^2(1 - \varepsilon^2). \quad (123)$$

Hence, the fluid cannot flow if

$$\begin{aligned} |M| < \frac{1}{2} \text{Max}\left(BH^2 - \frac{1}{4B}|\Sigma - \epsilon\kappa M + \frac{1}{2}H^2\Omega|^2, 0\right) \\ \rightarrow \frac{1}{2} \text{Max}\left(BH^2 - \frac{1}{4B}|\Sigma - \epsilon\kappa M|^2, 0\right) \end{aligned} \quad (124)$$

since $\Omega = 0$ where the fluid is rigid. The failure of (124) corresponds to a yield condition on the moment and extensional stress, given force and torque balance (which determine Σ and M) and the geometry (i.e. ϵ and κ).

Fig. 12 sketches the location of the yield condition on the $(|\Sigma - \epsilon\kappa M|, |M|)$ -plane. The condition corresponds to a locus parameterized by ε that is the union of a parabola (for $\varepsilon < 1$) and a piece of the $|\Sigma - \epsilon\kappa M|$ -axis (with $\varepsilon = 1$). Below this locus, in the shaded region, the fluid sheet is rigid. Thus, if one envisions a situation in which the stress on the sheet is slowly ramped up from zero, force and torque balance on each section of the rigid

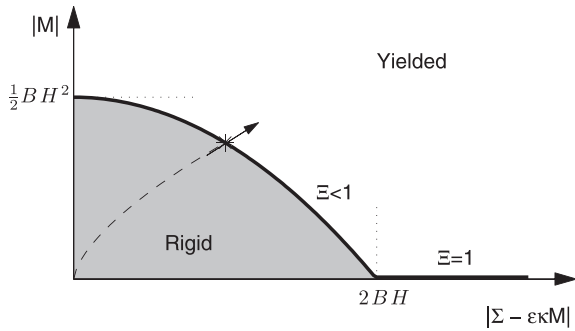


Fig. 12. Sketch of the yield condition in (124). The dashed line shows a sample pathway taken as the stress and torque upon a particular configuration are increased upto the yield point.

sheet dictate Σ and M , and identify a particular pathway taken upon the $(|\Sigma - \epsilon\kappa M|, |M|)$ -plane. When this path intersects the yield condition (as illustrated by the dashed curve and star in Fig. 12), the fluid yields, with a certain choice for Ξ then prescribed (and which determines the location of the neutral curve where σ_{ss} switches sign within the sheet).

Yielding through pure bending with no extensional stress corresponds to following a straight path from the origin inclined at an angle $\tan^{-1}(\epsilon\kappa)$. This reduces to a vertical path along the $|M|$ -axis for $\epsilon\kappa \rightarrow 0$, and recovers the yield criterion $|M| > \frac{1}{2}BH^2$ encountered in Section 3.4.1.

Yielding can, however, also occur without any bending whatsoever; this corresponds to a path along the $|\Sigma - \epsilon\kappa M|$ -axis with $M = 0$, and the condition in (124) then reduces to $|\Sigma| < 2BH$. This latter limit is relevant to an initially upright or vertically extruded viscoplastic column: the orientation of the sheet ($\theta = \pi/2$) guarantees that $M = 0$, whereas the force balance furnishes $\Sigma = -\epsilon GH(L - s)$. Hence the column yields at the base ($s = 0$) when the length L exceeds the threshold, $L_* = 2B/\epsilon G$, corresponding to a mode of compressive failure. Note that the order-one curvature theory of Section 3 is unable to account for this failure of the column, and unphysically predicts that a perfectly vertical beam never yields.

4.2. Euler buckling of a nearly vertical extrusion

We now return to the extrusion problem considered in Section 3.5, but focus on the situation that the beam is extruded almost vertically, rather than horizontally, creating an upright column. The boundary conditions remain as in (112)–(114), except that we now take $\theta_e \approx \frac{1}{2}\pi$. The full higher-order model in (116)–(121) can then be solved numerically, using a similar scheme to that described in Sections 3.4.2 and 3.5.2. A sample solution is shown in Fig. 13.

In this example, the column is extruded at speed $U_e = 1$ and has length $L_0 = L_* \equiv 2B/\epsilon G$ at $t = 0$. Thus, for $t > 0$ a small yielded section occurs adjacent to the point of extrusion where the compressive stress overwhelms the yield stress. If the extrusion angle is slightly off vertical, $0 < \theta_e - \pi/2 \ll 1$, bending then begins close to the extrusion, which eventually precipitates a sudden buckling of the column. During the buckling a large gravitational moment is generated, forcing almost the whole column to yield. Much of the fluid becomes rigid again once the column falls underneath the point of extrusion and hangs vertically downwards. Thereafter, the extensional stress remains sufficient to maintain a yielded section underneath the extrusion point, over which fluid continues to elongate and thin for longer times.

Initially, the yielded section remains small and the column effectively hinges about that boundary layer. The dynamics are controlled by the hinge in this phase of evolution, and we may

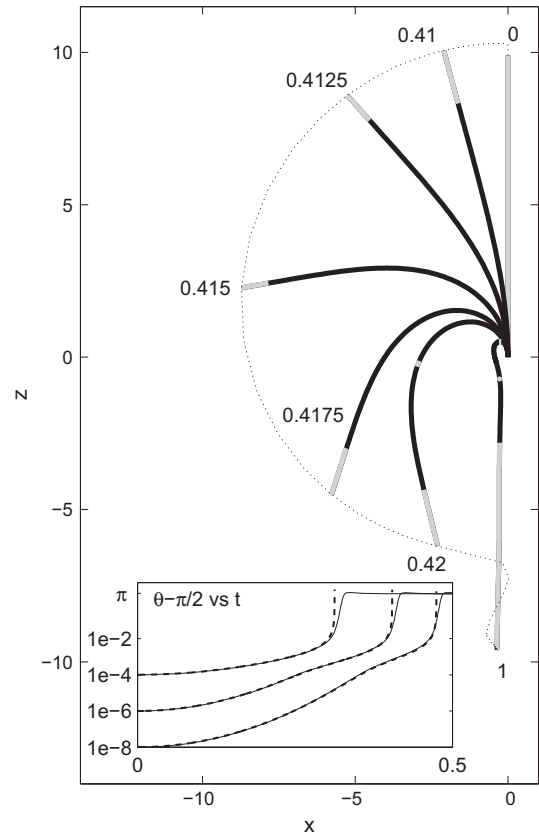


Fig. 13. Solutions for an extruded column with $B = 1$, $U_e = 1$, $G = 1$ and $\epsilon = 0.2$. The main image shows snapshots of the column at the times indicated (measured from the moment the length exceeds the critical length $L_* = 10$), for $\theta_e - \frac{1}{2}\pi = 10^{-6}$. Black and grey colouring denotes yielded and unyielded sections respectively and the dotted line shows the path of the free end. The inset shows the angle of the free end as a function of time for solutions with $\theta_e - \frac{1}{2}\pi = 10^{-4}$, 10^{-6} and 10^{-8} . In each case the dashed line shows the predictions of (131).

build an asymptotic solution exploiting our small parameter ϵ : we first observe that the bulk of the column rotates as a rigid shaft with angle $\theta(s, t) = \Theta(t)$. The force and torque balance in (116) and (117) then indicate that

$$\Sigma = -\epsilon G[L_* + t - s] \sin \Theta \tag{125}$$

and

$$M = -\frac{1}{2}G(L_* + t - s)^2 \cos \Theta. \tag{126}$$

To resolve the relatively narrow hinge and its small-time dynamics we introduce the rescalings

$$(s, t) = \epsilon(S, T), \quad (\theta, \Theta) = \frac{1}{2}\pi + \epsilon^4[\psi(S, T), \Psi(T)]. \tag{127}$$

The curvature over this region, $\kappa = \partial\theta/\partial s \rightarrow O(\epsilon^3)$, therefore remains relatively small, and imposing force and torque balance is equivalent to a reduction of (125) and (126):

$$\Sigma \sim -2B + \epsilon^2 G(S - T), \quad M \sim \frac{2}{G}\epsilon^2 B^2 \Psi. \tag{128}$$

By introducing these expressions into the yield condition (124), we determine the yield point,

$$S = T + \beta\Psi, \quad \text{where } \beta = \frac{4B^2}{G^2}. \tag{129}$$

For $0 \leq S \leq T + \beta\Psi$, the constitutive relations (120) and (121), then imply the scalings, $U \sim O(\epsilon)$, $W \sim O(\epsilon^4)$, $(\Delta, \Omega) \sim O(\epsilon^2)$ and

$\Xi \sim 1 + O(\epsilon^2)$. Thus, $\Delta \sim \epsilon^{-1}U_s$ and $\Omega \sim \epsilon^{-2}W_{ss}$, and a little more algebra furnishes

$$W_{ss} = \begin{cases} \frac{3}{2}\epsilon^4 G\beta\Psi, & S \leq \text{Max}(T - 3\beta\Psi, 0), \\ \frac{3}{8}\epsilon^4 G(T + \beta\Psi - S), & \text{Max}(T - 3\beta\Psi, 0) \leq S \end{cases} \quad (130)$$

(corresponding to $\Xi = 1$ and $\Xi < 1$, respectively). Integrating this expression from $S = 0$ (where $W_s = 0$) upto the yield point (129), where $W_s \rightarrow \epsilon^3 \partial\Psi/\partial T$, gives

$$\frac{\partial\Psi}{\partial T} = \begin{cases} \frac{3}{2}G\beta\Psi(T - \beta\Psi), & 3\beta\Psi \leq T, \\ \frac{3}{16}G(T + \beta\Psi)^2, & 3\beta\Psi > T. \end{cases} \quad (131)$$

The solutions of this equation blow up in finite time, corresponding to a catastrophic collapse of the column. The predictions of (131) are compared to full numerical solutions in Fig. 13 for three different extrusion angles, $\theta_e = \frac{1}{2}\pi + \epsilon^4\Psi(0)$. The initial angle, $\Psi(0)$, dictates the time taken to buckle.

Note that the dynamics captured by (131) is quite unlike that of a classical linear instability. Also, the scalings in (127) furnish an asymptotic solution to the beam model for small times. However, these scalings also undo the scaling that underscores the slender approximation itself, implying that the model may not be formally valid over this initial interval. It is hard to see how one could avoid this inconsistency whenever the beam yields over a sufficiently narrow region.

5. Discussion

In this paper we have presented three models describing the bending of a slender sheet of viscoplastic fluid. The first, suitable for relatively small curvature, is the analogue of classical elastic beam theory. The second describes order-one curvatures, along the lines of standard theories of elastic shells and viscous sheets. Our third model incorporates both small and order-one curvature within the same framework. In Appendix B, we extend the discussion and demonstrate that very similar models can be derived for circular threads. Thus, our viscoplastic solutions for falling catenaries, sagging and extruded beams, and buckling columns largely carry over to such three-dimensional settings (as in the flow problems of Fig. 1). Our results indicate that the gravitational fall of a viscoplastic sheet can be halted by the yield stress, or even prevented entirely. For extrusions, the yield stress prevents any deformation until a critical length is reached, whereafter dynamically evolving yielded zones mediate the distinctive drooping of a beam and the catastrophic collapse of an upright column.

The higher-order formulation in Section 4 also captures the extensional dynamics of a viscoplastic sheet. This accounts for compressional modes of failure, as well as yielding in pure bending, which is crucial in our example of the buckling column. The model also allows for long-time elongation and thinning, as the sheet or thread progresses towards a possible pinch-off, which properly demands the inclusion of surface tension. Indeed, the removal of bending from the higher-order thread model and the incorporation of the leading-order effects of surface tension renders that formulation equivalent to the theory of axisymmetric viscoplastic filaments presented by Balmforth, Dubash and Slim [1,2]. Thus, our formulation offers a compact description of slender viscoplastic sheets and threads in a wide range of physical settings. We leave open for future work the detailed application of the model to particular physical problems, as well as the generalization to fully three-dimensional viscoplastic plates and shells.

Appendix A. $O(\epsilon)$ contribution to Σ

Continuing the expansion of the velocities in (87) to $O(\epsilon^2)$ we find

$$w = W - \epsilon^2 n\Delta + \frac{1}{2}\epsilon^2 n^2\Omega + O(\epsilon^3),$$

$$u = U - \epsilon n(W_s + \kappa U) + O(\epsilon^3), \quad (A.1)$$

where Δ and Ω are as defined in (89), and hence

$$\dot{\gamma}_{ss} = 2(\Delta - n\Omega) + 4\epsilon\kappa n\Delta - 3\epsilon\kappa n^2\Omega + O(\epsilon^2). \quad (A.2)$$

The position at which $\dot{\gamma}_{ss}$ changes sign is

$$n = n_* \equiv \frac{\Delta}{\Omega} \left(1 + \frac{1}{2}\epsilon\kappa\Delta \right) + O(\epsilon^2). \quad (A.3)$$

Since $\tau_{ss} = \sigma_{ss} + p = \frac{1}{2}\sigma_{ss} - \frac{1}{2}\epsilon\sigma_{nn}$, the order ϵ correction to σ_{ss} includes a contribution from σ_{nn} , which is obtained from the leading-order form of the transverse force balance (76) and boundary conditions, $\sigma_{nn} = 0$ on $n = \pm\frac{1}{2}H$. One finds

$$\begin{aligned} \sigma_{nn} = & -4\kappa n\Delta - 2\kappa\Omega \left(\frac{1}{4}H^2 - n^2 \right) \\ & - 2\kappa B \text{sgn}(\Omega) \left[\text{Max}\left(\frac{1}{2}H, |n_*|\right) - |n_* - n| \right] + O(\epsilon), \end{aligned} \quad (A.4)$$

and

$$\begin{aligned} \sigma_{ss} = & 4(1 + \epsilon\kappa n)(\Delta - n\Omega) - \frac{1}{2}\epsilon\kappa H^2\Omega + 2B \text{sgn}(\dot{\gamma}_{ss}) \\ & - 2\epsilon\kappa B \text{sgn}(\Omega) \left[\text{Max}\left(\frac{1}{2}H, |n_*|\right) - |n_* - n| \right] + O(\epsilon^2). \end{aligned} \quad (A.5)$$

Integrating over the width, we arrive at the formulae quoted in (120) and (121). Note that, to be strictly accurate to $O(\epsilon)$, $\Xi = \text{Min}(1, |n_*|/\frac{1}{2}H)$. However, the $O(\epsilon)$ correction to n_* is only relevant when $\Sigma \sim O(\epsilon)$, in which case $\Delta \sim O(\epsilon)$ and the term $\frac{1}{2}\epsilon\kappa\Delta$ is smaller still. Thus, in Section 4 we retain only the leading order and write $\Xi = \text{Min}(1, |\Delta/H\Omega|)$.

Appendix B. The viscoplastic thread

Consider a thin thread moving under the action of gravity within the (x, z) -plane (precluding three-dimensional motions such as coiling [13]). As in Section 3, the centreline is described by $\mathbf{r}_c(s, t)$; s is arc length, n is the perpendicular coordinate in the (x, z) plane, and the third dimension is now represented by the coordinate y . The velocity components in the (s, y, n) coordinate system are denoted (u, v, w) , and the surface of the thread is located at $r \equiv \sqrt{y^2 + n^2} = R(s, \phi, t)$, where (r, ϕ) are polar coordinates in the plane perpendicular to the centreline; $n = r \cos \phi, y = r \sin \phi$. We assume that the thread is axisymmetric either to begin with or where it is extruded; as it turns out, the thread then remains axisymmetric to leading order from then on, and we may take $R = R(s, t)$.

The nondimensionalization is the same as in Section 3, scaling y and v in the same way as n and w , and setting

$$\hat{\tau}_{ij} = S^{-1}\tau_{ij}, \quad \hat{\sigma}_{ss} = S^{-1}\sigma_{ss}, \quad \epsilon\hat{\sigma}_{ij} = S^{-1}\sigma_{ij}, \quad (B.1)$$

where the last statement applies to all components except σ_{ss} . After dropping the hat decoration, the dimensionless equations of mass and momentum conservation are

$$\frac{\epsilon}{h} \frac{\partial u}{\partial s} + \frac{\partial v}{\partial y} + \frac{\partial w}{\partial n} - \frac{\epsilon \kappa}{h} w = 0, \quad (\text{B.2})$$

$$\frac{1}{h} \frac{\partial \sigma_{ss}}{\partial s} + \frac{\partial \sigma_{sy}}{\partial y} + \frac{\partial \sigma_{sn}}{\partial n} - \frac{2\epsilon \kappa}{h} \sigma_{sn} = \epsilon G \sin \theta, \quad (\text{B.3})$$

$$\frac{\epsilon}{h} \frac{\partial \sigma_{sy}}{\partial s} + \frac{\partial \sigma_{yy}}{\partial y} + \frac{\partial \sigma_{yn}}{\partial n} - \frac{\epsilon \kappa}{h} \sigma_{yn} = 0, \quad (\text{B.4})$$

$$\frac{\epsilon}{h} \frac{\partial \sigma_{sn}}{\partial s} + \frac{\partial \sigma_{yn}}{\partial y} + \frac{\partial \sigma_{nn}}{\partial n} + \frac{\kappa}{h} (\sigma_{ss} - \epsilon \sigma_{nn}) = \epsilon G \cos \theta, \quad (\text{B.5})$$

where $h = 1 - \epsilon n \kappa$ and $G = \rho g \mathcal{H} / \epsilon^2 S$, as in the main text. The free-stress boundary conditions on $r = R$ are

$$h \sigma_{sy} \sin \phi + h \sigma_{sn} \cos \phi - \epsilon \sigma_{ss} \partial R / \partial s = 0, \quad (\text{B.6})$$

$$h \sigma_{yy} \sin \phi + h \sigma_{yn} \cos \phi - \epsilon \sigma_{sy} \partial R / \partial s = 0, \quad (\text{B.7})$$

$$h \sigma_{yn} \sin \phi + h \sigma_{nn} \cos \phi - \epsilon \sigma_{sn} \partial R / \partial s = 0. \quad (\text{B.8})$$

The kinematic boundary condition may be written as

$$v \sin \phi + w \cos \phi = w_c \cos \phi + \epsilon \left[\frac{\partial R}{\partial t} + \frac{1}{h} \frac{\partial R}{\partial s} \left(u - u_c + \epsilon R \cos \phi \frac{\partial \theta}{\partial t} \right) \right], \quad (\text{B.9})$$

where w_c is the transverse velocity of the centreline.

The dimensionless constitutive law for the Bingham fluid is

$$\tau_{ij} = \dot{\gamma}_{ij} + B \dot{\gamma}_{ij} / \dot{\gamma}, \quad \text{if } \tau = \sqrt{\tau_{ss}^2 + \tau_{sn}^2} > B, \quad (\text{B.10})$$

and $\dot{\gamma}_{ij} = 0$ otherwise, where

$$\dot{\gamma}_{ss} = \frac{2}{\epsilon} \frac{\partial u / \partial s - \kappa w}{1 - \epsilon n \kappa}, \quad \dot{\gamma}_{yy} = \frac{2}{\epsilon^2} \frac{\partial v}{\partial y}, \quad \dot{\gamma}_{nn} = \frac{2}{\epsilon^2} \frac{\partial w}{\partial n},$$

$$\dot{\gamma}_{sn} = \frac{1}{\epsilon} \frac{\partial w / \partial s + \kappa u}{1 - \epsilon n \kappa} + \frac{1}{\epsilon^2} \frac{\partial u}{\partial n}, \quad \dot{\gamma}_{sy} = \frac{1}{\epsilon} \frac{\partial v / \partial s}{1 - \epsilon n \kappa} + \frac{1}{\epsilon^2} \frac{\partial u}{\partial y},$$

$$\dot{\gamma}_{yn} = \frac{1}{\epsilon^2} \left(\frac{\partial v}{\partial n} + \frac{\partial w}{\partial y} \right), \quad (\text{B.11})$$

The dimensionless pressure is $p = -\frac{1}{3}(\sigma_{ss} + \epsilon \sigma_{yy} + \epsilon \sigma_{nn})$, and the deviatoric stresses are given by

$$\tau_{ss} = \sigma_{ss} + p \rightarrow \frac{2}{3} \sigma_{ss}, \quad \tau_{yy} = \epsilon \sigma_{yy} + p \rightarrow -\frac{1}{3} \sigma_{ss},$$

$$\tau_{nn} = \epsilon \sigma_{nn} + p \rightarrow -\frac{1}{3} \sigma_{ss},$$

$$\tau_{sn} = \epsilon \sigma_{sn}, \quad \tau_{sy} = \epsilon \sigma_{sy}, \quad \tau_{yn} = \epsilon \sigma_{yn}. \quad (\text{B.12})$$

Thus, $(\dot{\gamma}_{ss}, \dot{\gamma}_{yy}, \dot{\gamma}_{nn}) \sim O(1)$, but $(\dot{\gamma}_{sn}, \dot{\gamma}_{sy}, \dot{\gamma}_{yn}) \sim O(\epsilon)$. As for the two-dimensional problem, this demands a certain form for the velocity field; in the current case

$$u = U - \epsilon n (W_s + \kappa U) + O(\epsilon^3), \quad (\text{B.13})$$

$$v = -\frac{1}{2} \epsilon^2 y \Delta + \frac{1}{2} \epsilon^2 n y \Omega + O(\epsilon^3), \quad (\text{B.14})$$

$$w = W - \frac{1}{2} \epsilon^2 n \Delta + \frac{1}{4} \epsilon^2 (n^2 - y^2) \Omega + O(\epsilon^3), \quad (\text{B.15})$$

where the stretching rate Δ and bending rate Ω are defined as in (89). Thus, $\dot{\gamma}_{ss} = 2(\Delta - n\Omega) + O(\epsilon)$ and

$$\sigma_{ss} = 3(\Delta - n\Omega) + \sqrt{3} B \text{sgn}(\Delta - n\Omega) + O(\epsilon). \quad (\text{B.16})$$

We may now calculate the leading order expressions for the resultant extensional stress and bending moment:

$$\Sigma = \int_A \sigma_{ss} dA, \quad M = \int_A n \sigma_{ss} dA, \quad (\text{B.17})$$

where the integrals are taken over the circular cross section in the plane perpendicular to the centreline. Thence, when the fluid is yielded,

$$\Sigma = 3\pi R^2 \Delta + 2\sqrt{3} B R^2 \left[\sin^{-1} \Xi + \Xi(1 - \Xi^2)^{1/2} \right] \text{sgn}(\Delta) \quad (\text{B.18})$$

and

$$M = -\frac{3}{4} \pi R^4 \Omega - \frac{4}{\sqrt{3}} B R^3 (1 - \Xi^2)^{3/2} \text{sgn}(\Omega), \quad (\text{B.19})$$

where

$$\Xi = \text{Min}(1, |\Delta / R\Omega|). \quad (\text{B.20})$$

Integrals of the force balance Eqs. (B.3)–(B.5) give, to $O(\epsilon^2)$,

$$\frac{\partial \Sigma}{\partial s} - \epsilon \kappa \frac{\partial M}{\partial s} = \epsilon G A \sin \theta, \quad (\text{B.21})$$

$$\epsilon \frac{\partial M}{\partial s} + \kappa \Sigma = \epsilon G A \cos \theta, \quad (\text{B.22})$$

where $A = \pi R^2$ is the cross-sectional area. The integrated mass conservation equation is

$$\frac{\partial A}{\partial t} + \frac{\partial}{\partial s} (A \bar{U}) = 0, \quad \frac{\partial \bar{U}}{\partial s} = \epsilon \Delta, \quad (\text{B.23})$$

where $\bar{U} = U - u_c$ is the velocity of the fluid relative to the centreline. Finally, the centreline evolution Eq. (80) again reduces to (102).

As for the two dimensional sheet, when $\kappa = O(1)$ the force balance equations demand $\Sigma = O(\epsilon)$ and hence, from (B.18), $\Delta \sim O(\epsilon)$ and $\Xi \sim O(\epsilon)$. Eq. (B.19) then simplifies to

$$M = -\frac{3A^2 \Omega}{4\pi} - \frac{4BA^{3/2}}{\pi\sqrt{3}\pi} \text{sgn}(\Omega), \quad \text{if } |M| > \frac{4BA^{3/2}}{\pi\sqrt{3}\pi}, \quad (\text{B.24})$$

and $\Omega = 0$ otherwise. In the other extreme, when there is no bending (i.e. for a vertical thread), $\kappa = \Omega = 0$, $\Delta = U_s$, and (B.18) simplifies to

$$\Sigma = 3A\Delta + \sqrt{3}BA \text{sgn}(\Delta), \quad \text{if } |\Sigma| > \sqrt{3}BA, \quad (\text{B.25})$$

and $\Delta = 0$ otherwise.

References

- [1] N.J. Balmforth, N. Dubash, A. Slim, Extensional dynamics of viscoplastic filaments: I. Long-wave approximation and the Rayleigh instability, *J. Non-Newt. Fluid Mech.* 165 (2010) 1139–1146.
- [2] N.J. Balmforth, N. Dubash, A. Slim, Extensional dynamics of viscoplastic filaments: II. Drips and bridges, *J. Non-Newt. Fluid Mech.* 165 (2010) 1147–1160.
- [3] J.D. Buckmaster, A. Nachman, L. Ting, The buckling and stretching of a viscida, *J. Fluid Mech.* 69 (1975) 1–20.
- [4] I. Howell, Models for thin viscous sheets, *Eur. J. Appl. Math.* 7 (1996) 321–343.
- [5] K. Kamrin, L. Mahadevan, Soft catenaries, *J. Fluid Mech.* 691 (2012) 165–177.
- [6] J.P. Koulakis, C.D. Mitescu, F. Brochard-Wyart, P.-G. de Gennes, E. Guyon, The viscous catenary revisited: experiments and theory, *J. Fluid Mech.* 609 (2008) 87–110.
- [7] A.E.H. Love, *The Mathematical Theory of Elasticity*, Dover, 1944.
- [8] J. Lubliner, *Plasticity Theory*, Dover, 2008.
- [9] L. Mahadevan, J.B. Keller, Periodic folding of thin sheets, *SIAM Rev.* 41 (1999) 115–131.
- [10] W. Prager, P.G. Hodge, *Theory of Perfectly Plastic Solids*, Wiley, 1951.
- [11] N.M. Ribe, Buckling and stretching of thin viscous sheets, *J. Fluid Mech.* 433 (2001) 135–160.
- [12] N.M. Ribe, Periodic folding of viscous sheets, *Phys. Rev. E* 68 (2003) 036305.
- [13] N.M. Ribe, Coiling of viscous jets, *Proc. Roy. Soc. Lond. A* 460 (2004) 3223–3239.
- [14] G.I. Taylor, Instability of jets, threads and sheets of viscous fluid, *Proc. 12th Intern. Conf. Appl. Mech.* (1969) 382–389.
- [15] J. Teichman, L. Mahadevan, The viscous catenary, *J. Fluid Mech.* 478 (2003) 71–80.
- [16] L.N. Trefethen, *Spectral Methods in MATLAB*, SIAM, 2000.